J. metamorphic Geol., 2007, **25,** 803–827 doi:10.1111/j.1525-1314.2007.00729.x

Permian to Cretaceous polymetamorphic evolution of the Stewart River region, Yukon-Tanana terrane, Yukon, Canada: *P–T* evolution linked with *in situ* SHRIMP monazite geochronology

R. G. BERMAN,[1] J. J. RYAN,[2] S. P. GORDEY[2] AND M. VILLENEUVE[1]
[1]*Geological Survey of Canada, 615 Booth St., Ottawa, Ontario, Canada K1A 0E9 (rberman@nrcan.gc.ca)*
[2]*Geological Survey of Canada, 625 Robson Street, Vancouver, British Columbia, Canada V6B 5J3*

ABSTRACT Textural relationships and the trace element chemistry of accessory minerals and garnet can provide the linkage between *in situ* SHRIMP ages and quantitative pressure–temperature data that is required to decipher complex polymetamorphic and polydeformational histories. Application of these methods to lower amphibolite facies rocks of the Stewart River area, Yukon (Canada) yields robust new constraints on the tectonic evolution of central Yukon Tanana Terrane (YTT). A TIMS U/Pb titanite age of 365–350 Ma is interpreted to date low-*P* metamorphism (M1) and D1 deformation associated with arc plutonism above an east-dipping subduction zone. Monazite inclusions in garnet porphyroblasts record a transition from low to high pressure (~9 kbar and 600 °C) at *c.* 239 Ma. These data help to establish a *c.* 260–240 Ma tectonometamorphic event (M2–D2) reflecting intra-arc thickening during west-dipping subduction of Slide Mountain Ocean. Another transition from low- to high-*P* (M3–D3; 7.8 kbar and 595 °C), dated by *c.* 195–187 Ma monazite, is interpreted to reflect the change from regional contact metamorphism during arc plutonism to internal duplication of YTT during initial collision of YTT with the North American craton. The Mt Burnham (north-eastern) region records a different history because of its proximity to later plutons and its late exhumation via extensional faulting. Monazite growth at 146 Ma dates ~9 kbar metamorphism (M4), interpreted to reflect a previously unrecognized period of plutonism associated with auriferous quartz veins in the Klondike region. Monazite growth at 114–107 Ma reflects low-*P* (< 4.6 kbar) contact metamorphism (M5) accompanying regional plutonism and extension.

Key words: *in situ* geochronology; *P–T* data; SHRIMP; tectonics; Yukon-Tanana.

INTRODUCTION

Recent advances in metamorphic dating techniques have made it possible to gain important new insights into metamorphic processes and histories by establishing the age of not only specific porphyroblasts and associated *P–T* conditions (e.g. Zhu *et al.*, 1997; Foster *et al.*, 2002, 2004; Berman *et al.*, 2005 and references therein), but also metamorphic reactions (e.g. Gibson *et al.*, 2004; Kohn & Malloy, 2004) and deformation fabrics (Williams *et al.*, 2002; Berman *et al.*, 2005). In polymetamorphic rocks, these applications are hampered by the difficulty in linking different generations of accessory minerals (e.g. monazite, zircon) to specific textural or chemical features of rocks. Here this problem is addressed with *in situ* SHRIMP data for polymetamorphic rocks of Yukon-Tanana terrane (YTT), and the use of textural relationships combined with the chemistry of accessory minerals and garnet to help decipher complex polymetamorphic and polydeformational histories.

A major constituent of the northern North American Cordillera, YTT consists of Palaeozoic and Mesozoic, variably metamorphosed and deformed igneous and sedimentary rocks that were emplaced as an allochthonous sheet above strata of the ancestral North American margin (Tempelman-Kluit, 1979). To date, regional metamorphic data with which to constrain this tectonic history are available only for YTT in Alaska, where moderate- to high-*P* (7–12 kbar) amphibolite facies metamorphism (Dusel-Bacon *et al.*, 1995) is constrained largely by ^{40}Ar-^{39}Ar cooling ages (Dusel-Bacon *et al.*, 2002). In Yukon, metamorphic studies of YTT focused on small-scale studies of crustal rocks (Johnston *et al.*, 1996; Stevens, 1996) and on scattered eclogite occurrences (Fig. 1; Creaser *et al.*, 1997; Erdmer *et al.*, 1998; Fallas *et al.*, 1999; Perchuk *et al.*, 1999; Devine *et al.*, 2006) within tectonic slices along the boundaries of YTT, which are not representative of the terrane as a whole.

Here this sparse metamorphic data set is augmented with a metamorphic and geochronological study that is integrated with detailed and systematic mapping of YTT in the Stewart River area of west-central Yukon, Canada (Fig. 1). *In situ* SHRIMP U-Pb monazite ages are linked to changing *P–T* conditions, thus providing robust metamorphic constraints for interpretation of the tectonic evolution of this region.

© 2007 Blackwell Publishing Ltd

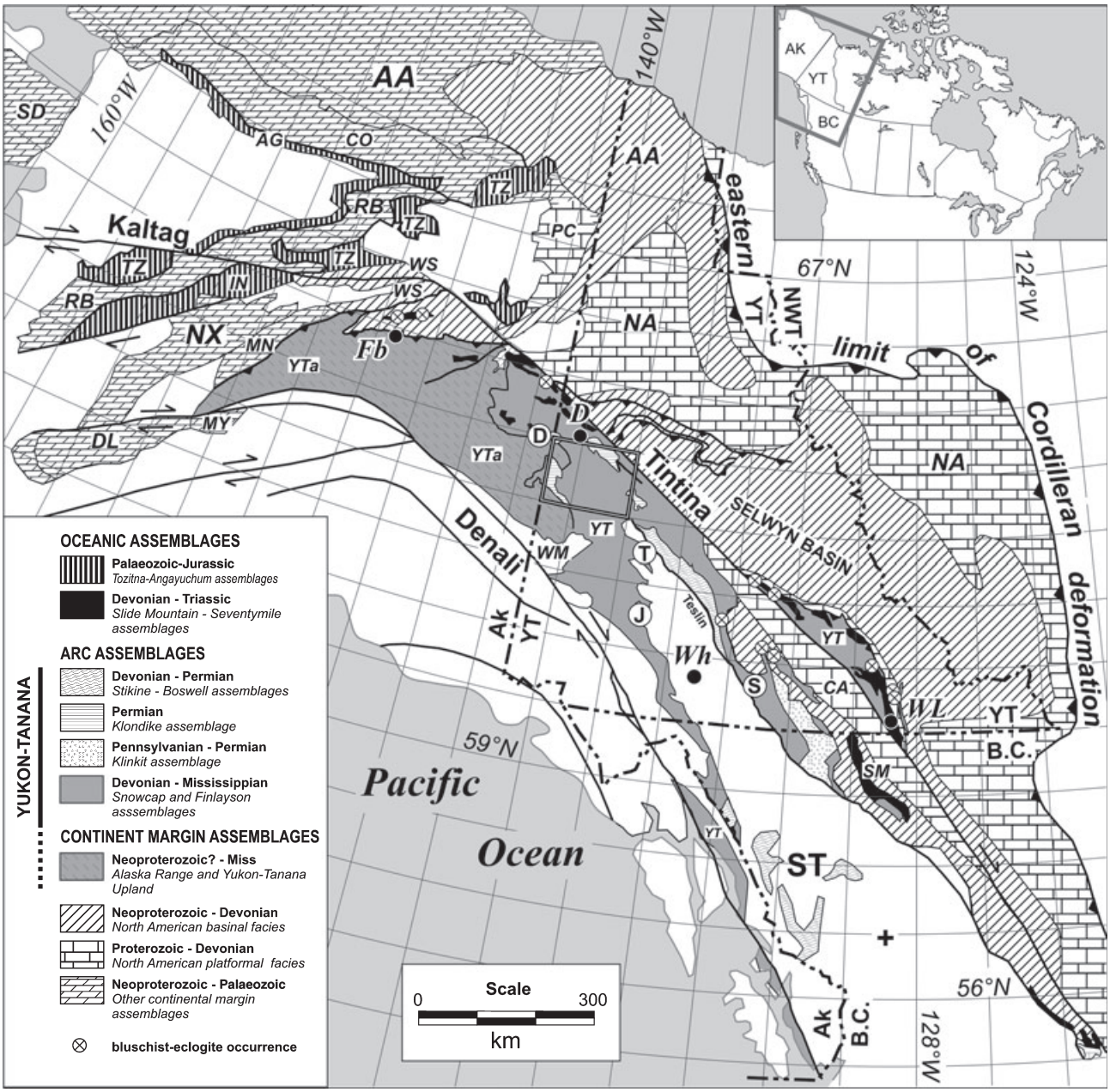
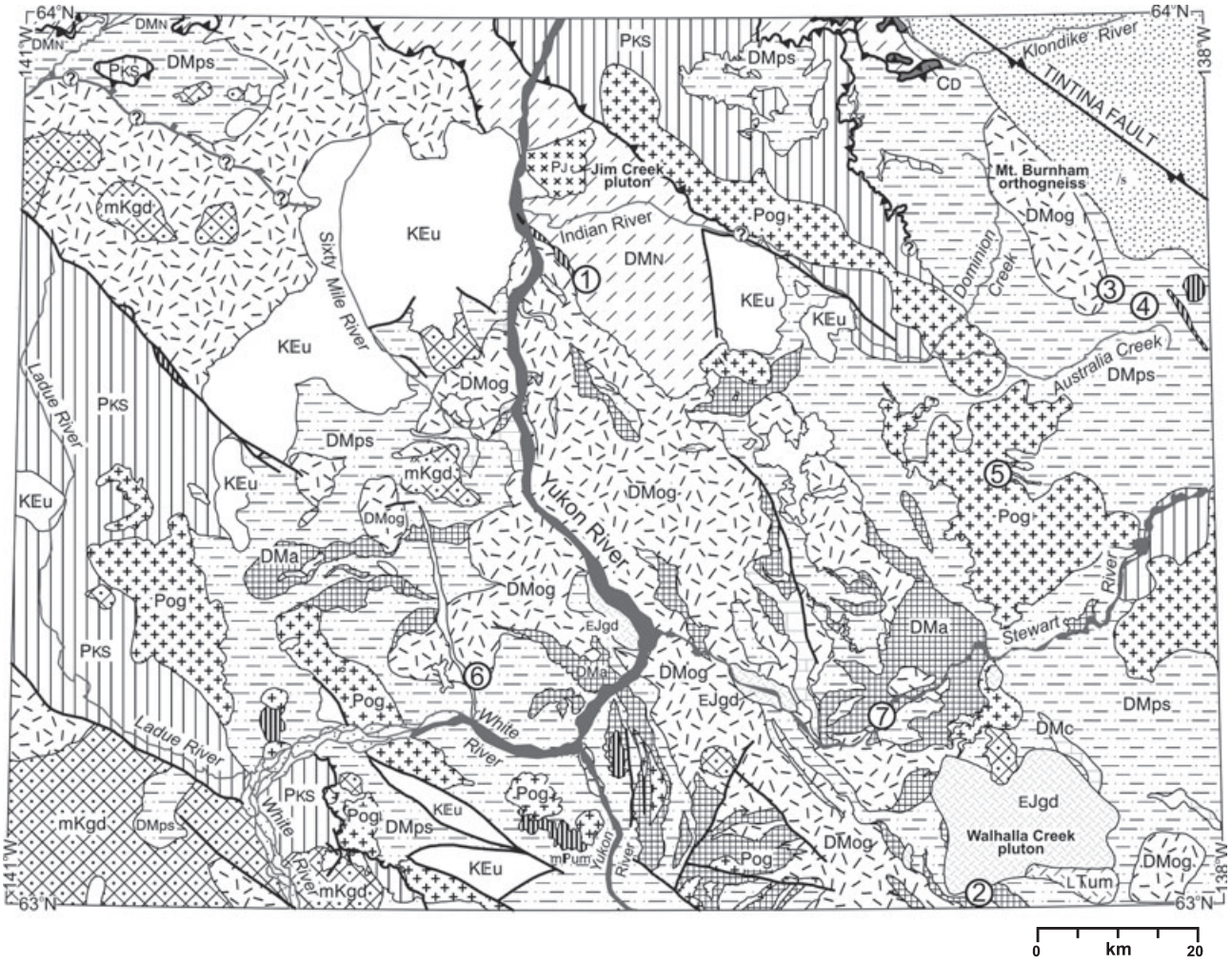


Fig. 1. Geological setting of Stewart River area (area of Fig. 2) with respect to Palaeozoic tectonic assemblages of northern Cordillera (modified from Colpron *et al.*, 2006a,b, Fig. 4). Circled letters show locations of studies referred to in text: J = Johnston *et al.* (1996); T = Tafti & Mortensen (2004); S = Stevens (1996); D = Dusel-Bacon *et al.* (1995). Lithotectonic terranes and assemblages: AA – Arctic Alaska (includes Endicott Mountains, North Slope and Skajit allochthon); AG – Angayucham; BS – Boswel-Seminof; CA – Cassiar; CO – Coldfoot (schist belt of southern Brooks Range); DL – Dillinger; IN – Innoko; MN – Minchumina; MY – Mystic; NA – North American miogeocline; NX – Nixon Fork; PC – Porcupine; RB – Ruby; SD – Seward; SM – Slide Mountain-Seventymile; ST – Stikine (Asitka); TZ – Tozitna; WM – Windy-McKinley; WS – Wickersham; YT – Yukon-Tanana in easternmost Alaska, Yukon and B.C.; YTa – possibly Yukon-Tanana (as formerly assigned), recently interpreted as parautochthonous North America by Dusel-Bacon *et al.* (2006). Political divisions: AK – Alaska; YT – Yukon; B.C. – British Columbia; NWT – Northwest Territories; Towns: D – Dawson; Fb – Fairbanks; Wh – Whitehorse; WL – Watson Lake.

STEWART RIVER AREA

YTT in the Stewart River area (Fig. 2), consists of Palaeozoic, twice-transposed, amphibolite facies gneiss and schist which represent, at a regional scale, some of the most thoroughly reworked rocks within the terrane (Fig. 1; Ryan & Gordey, 2001, 2002; Ryan *et al.*, 2003; Gordey & Ryan, 2005). These are pierced by younger plutonic or hypabyssal intrusions of Late Triassic, Jurassic, Cretaceous and Eocene age (Gordey & Ryan,

© 2007 Blackwell Publishing Ltd



QUATERNARY

/s — fluvial silt, sand and gravel

CRETACEOUS TO EOCENE

KEu — undifferentiated sedimentary and volcanic cover

MID-CRETACEOUS

mKgd — syenogranite to monzogranite; biotite-hornblende granodiorite

EARLY JURASSIC

EJgd — biotite hornblende granodiorite, monzogranite, quartz monzonite and quartz monzodiorite

LATE TRIASSIC

LTum — pyroxenite, minor hornblendite

sample site: ⑦

fault — high angle; thrust, teeth on upper plate; dextral

CARBONIFEROUS

CD — ***Dawson-Clinton Creek Assemblage:*** greenstone, serpentinite, harzburgite

MID- TO LATE PALAEOZIC

mPum — amphibolite facies metagabbro, metapyroxenite and altered equivalents, including serpentininte and talc-siderite schist

PERMIAN

PKS — ***Klondike Schist:*** muscovite-chlorite-quartz-feldspar schist, chlorite schist, chlorite phyllonite

PJ — ***Jim Creek Pluton:*** biotite granite to quartz monzonite, commonly K-feldspar megacrystic; lacks structural fabric

Pog — K-feldspar rich granite to quartz monzonite orthogneiss, K-feldspar augen orthogneiss, minor tonalite orthogneiss

DEVONIAN TO MISSISSIPPIAN

DMN — ***Nasina Assemblage:*** black carbonaceous quartzite and metapelite; minor marble

DMog — K-feldspar rich granite orthogneiss and K-feldspar augen orthogneiss; intermediate to mafic biotite-hornblende tonalitic orthogneiss, commonly with interlayed amphibolite and mafic schist

DMa — amphibolite schist and gneiss, garnet amphibolite

DMc — marble

DMps — quartz-garnet-biotite-muscovite schist with lenses to mappable members of micaceous quartzite; minor metaconglomerate

Fig. 2. Simplified geology of Stewart River area (after Gordey & Ryan, 2005). Circled numbers show sample locations 1–7. Grey fault with question marks in the north-west shows extensional fault (ornament on upper plate) of Dusel-Bacon *et al*. (2002).

© 2007 Blackwell Publishing Ltd

2005), and overlain by Upper Cretaceous volcanic rocks, local Lower Cretaceous conglomerate, and rare Quaternary basalt. Unmetamorphosed Palaeozoic strata of the ancestral North American margin lie immediately across the Tintina Fault to the north-east (Fig. 1). The latest Cretaceous to Tertiary dextral displacement across the fault has shifted the Stewart River area 400–430 km north-westerly from YTT counterparts in the Finlayson Lake area of south-central Yukon (Gabrielse *et al.*, 2006).

Devonian to Mississippian assemblage

The lowermost unit in the Stewart River area (Ryan & Gordey, 2001, 2002; Ryan *et al.*, 2003) consists of widespread metasiliciclastic rocks that are dominated by psammite and quartzite, with lesser pelite and rare conglomerate (DMps, Fig. 2). Preliminary geochronology suggests a Middle Palaeozoic age (Villeneuve *et al.*, 2003), and correlation with the Snowcap assemblage elsewhere in YTT (Colpron *et al.*, 2006a). Intermediate to mafic composition amphibolite (DMa) derived from volcanic rocks with arc tholeiitic affinities (Piercey *et al.*, 2006) interdigitates with, and lies stratigraphically above, the siliciclastic rocks. Marble (DMc) occurs within both the amphibolite and siliciclastic rocks. In turn, grey carbonaceous quartzite, metapelite and minor marble of the Nasina assemblage (DMN), largely devoid of volcanic-derived material, lie structurally above and/or may be partly equivalent to the aforementioned metaclastic rocks.

The amphibolite and metasiliciclastic rocks are intruded by Late Devonian to Early Mississippian (Villeneuve *et al.*, 2003; Ruks *et al.*, 2006) calcalkalic (Piercey *et al.*, 2006; Ruks *et al.*, 2006), metaluminous granitoids (now orthogneiss) with diorite, tonalite, granodiorite, monzogranite and granite protoliths. The metaplutonic rocks are interpreted to have formed the core of an arc, with the amphibolite representing its volcanic carapace. Plutonic rocks of similar age are widely recognized elsewhere in YTT as the Simpson Range plutonic suite (Colpron *et al.*, 2006a). Detrital zircon analysis demonstrate that some quartzites (probably correlative with the Pelmac Quartzite; Colpron *et al.*, 2006b) were deposited synchronously with this Mississippian plutonic suite (Villeneuve *et al.*, 2003), indicating an unconformity within the amphibolite and metasiliciclastic rocks.

Permian succession

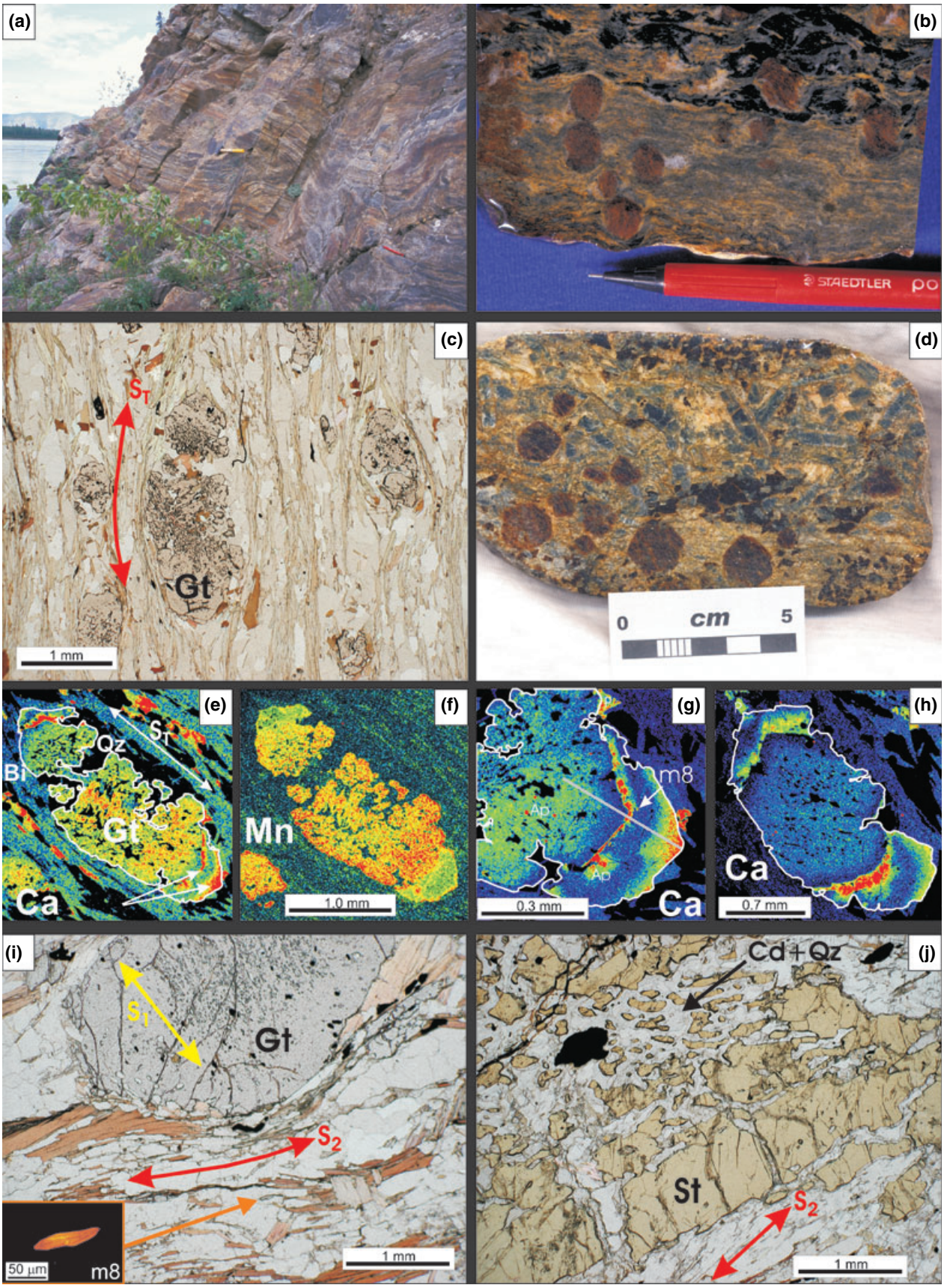
Overlying the Devonian and Mississippian rocks in the western and north-eastern parts of the map area is the Klondike schist (Fig. 2, PKS), a highly fissile, muscovite-quartz and chlorite-quartz schist, derived primarily from Permian volcanic and volcaniclastic protoliths (Mortensen, 1992), and the dominant rock type in the renowned Klondike placer mining district. Permian porphyritic granite orthogneiss bodies are considered plutonic to subvolcanic equivalents (Ruks *et al.*, 2006) of the schist. In the north-east, Permian granite orthogneiss apparently intrudes the contact between the Klondike schist and Devonian–Mississippian rocks, suggesting an unconformable(?) contact that is not significantly displaced by later tectonism. In most places, however, the nature of the boundary is obscured by the high state of regional strain.

Structural summary

Palaeozoic rocks in the Stewart River area exhibit a regional foliation (S_T) that is characterized by high-strain transposition of layering in gneisses and schists, with abundant intrafolial isoclinal folds that are commonly rootless (Fig. 3a). Prior to regional F3 folding, S_T had a shallowly dipping orientation. Primary compositional layering (S0) in metasedimentary rocks, unit contacts (e.g. dyke margins), and a pre-existing foliation (S1) can be traced around closures of recumbent to shallowly inclined, close to isoclinal, long-wavelength folds (F2). Associated with these folds is an intensely developed regional extension lineation (L2) that is parallel to the F2 axes. Surprisingly, even at these high strains, there is little development of an axial planar fabric; rather, S_T is characterized by the complete reorientation of, and strain intensification of S0 and S1. The present geometrical surface of S_T is considered largely a second-generation feature that is generally referred to here as S2, although there is evidence (e.g. sample 1) for its local reactivation during D3. D3 is most evident as open, moderately inclined (with shallow to steep varieties), shallowly plunging F3 folds that have a weak axial–planar fabric developed in schistose layers, and generally have no associated extension lineation. While they have been observed locally throughout most of the area, F3 structures are not present everywhere. Some localities exhibit a

Fig. 3. (a) Large-scale isoclinal, shallowly dipping F2 transposition folds of an S1 gneissosity within mixed metasedimentary gneiss with granitic veins. (b) Polished rock slab of Grt-Hbl-Ms schist derived from intermediate composition volcaniclastic metasedimentary rock. Garnet contains internal fabric (S1?) at an angle to the foliation (S2) which envelops garnet. Sample 00RAY-20-35. (c) Photomicrograph of sample 1, with S_T (S2 + S3) enveloping garnet porphyroblasts (garnet no. 1 is the largest) that are elongate parallel to S_T. (d) Polished rock slab of sample 2. Garnet, kyanite, and staurolite overgrow the main foliation (S2). (e–h) X-ray maps of garnet porphyroblasts in sample 1: (e) Ca, (f) Mn, (g) Ca (close-up of rim shown in e) in garnet no. 1; grey line is traverse line shown in Fig. 4a; (h) Ca in different garnet porphyroblast. Concentration increases through the colour spectrum from blue to red. Highest Ca minerals are apatite (Ap) inclusions in garnet and matrix plagioclase (P). White arrows in (e) show location of two high-Ca spikes. (i) Photomicrograph of sample 3, with S2 wrapping garnet porphyroblasts with internal fabric at a high angle to S2. Inset shows yttrium X-ray map of elongate matrix monazite (no. 8). (j) Photomicrograph of sample 4, with staurolite porphyroblast overgrowing S2 and partially replaced by intergrowths of cordierite and quartz.

© 2007 Blackwell Publishing Ltd



© 2007 Blackwell Publishing Ltd

moderately inclined to upright spaced (1–3 cm) S3 cleavage, overprinting F2 isoclines. D3 is older than Lower Cretaceous, because it is not present in conglomerates of this age.

Regional metamorphism

Peak metamorphic grade in the Stewart River area is generally lower to middle amphibolite facies, with Devono-Mississippian rocks displaying Grt-St-Ky-Ms (abbreviations after Kretz, 1983) in rare metapelites and Grt-Hbl in metavolcanic rocks. The Klondike schist is largely greenschist facies, but chlorite-biotite mats pseudomorphing finger-sized hornblende in the south-eastern part of the schist suggest that its lower grade is retrograde in origin, reflecting enhanced permeability of the schists during later metamorphic events. In metasedimentary rocks, retrograde effects are localized and generally restricted to partial breakdown of garnet to biotite and/or chlorite.

The relationship between fabric development and metamorphic mineral growth is complex in hand samples and at the microscopic scale (Fig. 3b–j). Locally, garnet is wrapped by S2 and overgrows an internal fabric (S1) at a high angle to S2 (Fig. 3b,c,i). In some cases, S2 is overgrown by garnet (Fig. 3d) and rarely staurolite, suggesting a post-S2 metamorphic event. Similarly, amphibolites south of Thistle Creek show two populations of hornblende, both of which yield *c*. 180 Ma cooling ages (Villeneuve *et al*., 2003). An older set defines the regional stretching lineation, whereas coarse (5–50 mm) rosettes radiate within, and locally across, the foliation plane. A detailed description is provided of textural relationships as well as quantitative metamorphic conditions for representative samples, some of which were also used for *in situ* SHRIMP geochronology.

PETROLOGICAL METHODS

Thermobarometry

Selected mineral compositions for *P–T* estimates were determined using a Cameca SX-50 electron microprobe at the Geological Survey of Canada (Ottawa), employing four spectrometers, a range of natural and synthetic standards, and matrix corrections after Pouchou & Pichoir (1985). Analytical conditions for all phases were 20 kV accelerating voltage, with a 10-nA beam current. A 10-μm beam spot was used for feldspars and a more focused beam ($\sim$3 μm) for garnet, biotite, staurolite and muscovite.

Pressure–temperature estimates were obtained using the TWEEQU software (Berman, 1991; http://gsc.nrcan.gc.ca/sw/twq_e.php) to calculate the following independent set of equilibria from internally consistent thermodynamic data:

$$3\mathrm{An} = \mathrm{Grs} + 2\mathrm{Ky} + \mathrm{Qtz} \quad (1)$$

$$\mathrm{Ann} + \mathrm{An} = \mathrm{Grs} + \mathrm{Alm} + \mathrm{Ms} \quad (2)$$

$$\mathrm{Ann} + \mathrm{Prp} = \mathrm{Phl} + \mathrm{Alm} \quad (3)$$

$$12\mathrm{Qtz} + 3\mathrm{Ts} + 2\mathrm{Prp} + 4\mathrm{Grs} = 12\mathrm{An} + 3\mathrm{Tr} \quad (4)$$

$$3\mathrm{Tr} + 5\mathrm{Alm} = 5\mathrm{Prp} + \mathrm{FeTr} \quad (5)$$

In addition to equilibrium (5), the model of Holland & Blundy (1994) was used for thermometry of amphibolite samples with the equilibrium:

$$\mathrm{Ed} + 4\mathrm{Qtz} = \mathrm{Tr} + \mathrm{Ab} \quad (6)$$

TWEEQU calculations were performed with version 1.02, which incorporates the following activity models relevant to the above equilibria: Fuhrman & Lindsley (1988) for plagioclase, Chatterjee & Froese (1975) for muscovite, Berman (1990) for garnet, McMullin *et al*. (1991) for biotite, and Mader *et al*. (1994) for amphibole. For samples 2 and 4 with sodic plagioclase, the calculations used the plagioclase model of Aranovich (1991), which yields lower pressures for sodic plagioclase which are generally more consistent with independent estimates (Aranovich, 1991). Absolute errors of thermobarometric data are considered to be approximately ± 50 °C and 1 kbar (Berman, 1991), with appreciably smaller errors associated with relative differences between samples of similar bulk composition.

Phase diagram calculations

In order to help constrain *P–T* conditions and *P–T–t* paths during multiple metamorphic events, the program DOMINO (de Capitani, 1994; http://titan.minpet.unibas.ch/minpet/theriak/theruser.html; August 2003 version) was used to calculate phase relationships in the system MnO-CaO-Na_2O-K_2O-FeO-MgO-Al_2O_3-SiO_2-H_2O. The calculations were based on compositions determined by X-ray fluorescence analyses of powdered rock samples derived from the offcuts of polished thin sections used to obtain mineral analyses via microprobe. All calculations used the thermodynamic data set of Holland & Powell (1998), which includes Mn end-members. Activity–composition models employed in this study are summarized by Tinkham *et al*. (2001), with the biotite and chlorite models re-parameterized for use with DOMINO (C. de Capitani, pers. comm.). Saturation with pure H_2O was assumed for all calculations.

QUANTITATIVE METAMORPHIC CONSTRAINTS

Quantitative estimates of metamorphic conditions were evaluated using the inverse and forward modelling techniques presented above. In order to link *P–T* and timing constraints, samples of metasedimentary rocks were chosen that contained monazite suitable for

© 2007 Blackwell Publishing Ltd

Table 1. Summary of thermobarometric and geochronological data.

No.	Field no.	Lab. no.	UTM (zone 7) Easting	Northing	Main assemblage	P^a (kbar)	T^a(°C)	Eq.[b]	Age[c] (Ma)	Interpretation
7	01-VN-01	7039	608940	7011484	Hbl-Pl-Cc-Ttn				*c.* 365–350	M1–D1 tm
									c. 265	M2–D2 tm
5	03-RAYR-036A1		622732	7041763	Grt-Hbl-Bt-Pl-Qtz	9.8	615	4,5,7		M2–D2 (?) tm
6	03-GGAR-175A1		558218	7015139	Grt-Hbl-Ep-Pl-Qtz	9.5	665	4,5,7		M2–D2 (?) tm
1	03-RAY-028A1	8509	570634	7065082	Grt-Ms-Bt-Pl-Qtz	~9	~600	pd	239 ± 7	M2–D2 low- to high-*P* tm
						7.8	595	2,3	187 ± 5	M3–D3 low- to high-*P* cm (post-peak *T*)
2	01-RAY-GR-1	8506	621950	6990797	Grt-Ky-St-Pl-Qtz	5.4	~600	1,6	195 ± 2	M3–D3 low-*P* cm (prograde)
						7.6	~600	1,6		M3–D3 high-*P* cm (near-peak *T*)
4	03-RAY-P003A1	8507	640469	7063436	Grt-Bt-St-Ky-Pl-Qtz-Crd	8.9	610	1,3	146 ± 3	M_4 high-*P* cm
						4.6	600	pd	107 ± 2	M_5 low-*P* cm
3	03-RAY-P013A1	8508	635836	7065506	Grt-St-Ky-Ms-Bt-Pl-Qtz	~9	~500	pd		M1–D1 tm
						~9	~620	pd		M2–D2 tm
						< 6.1	< 590	1,3	114 ± 2	M_5 low-*P* cm; extensional deformation

Samples are listed in chronological order, with numbers corresponding to their order discussed in the text.
tm, tectonometamorphism; cm, contact metamorphism.
[a]Estimated uncertainties are ± 1 kbar and 50 °C (Berman, 1991).
[b]Equilibria used to derive listed *P–T* values (pd = phase diagram constraints).
[c]All ages determined by *in situ* SHRIMP analysis of monazite, except for sample 7 (TIMS titanite data).

SHRIMP analysis. This requirement severely limited sample choice, as most metasedimentary rocks were either barren with respect to monazite, or contained grains < 10 μm in the shortest dimension. Of the four selected samples, three were from the eastern part of the area and one from the north-central part. In order to provide more complete regional coverage, and to compare *P–T* results of different bulk composition rocks, *P–T* data were also obtained for two metavolcanic rocks (garnet amphibolite) in the western part of the area. Table 1 summarizes thermobarometric and geochronological results in relation to inferred metamorphic and deformation events. Table 2 gives the compositions of minerals used for thermobarometric calculations.

Sample 1

Sample 1 is a Grt-Bt-Ms-Pl-Qtz schist from the southern extent of the Nasina assemblage (Fig. 2). Although kyanite is present in nearby outcrops, sample 1 shows no evidence of relic aluminosilicate or staurolite. Syntectonic garnet growth is indicated by elongate porphyroblasts, up to 0.5 × 1.5 mm in size, that are enveloped by the regional transposition fabric (S_T) defined by biotite, muscovite and aggregates of elongate plagioclase and quartz (Fig. 3c). Most porphyroblasts display irregular, partially resorbed core regions with internal fabrics defined by quartz, ilmenite, apatite and rutile inclusions at a high angle to S_T (Fig. 3c, e–h). In some porphyroblasts, the garnet core comprises domains with different orientations of internal fabric, suggesting coalescence of variably rotated, early (M1) garnet grains after overgrowth of the early (S1) fabric. In contrast to partially resorbed M1 cores, most garnet porphyroblasts display subhedral to euhedral, inclusion-poor rims that are particularly well developed in S_T pressure shadows (Fig. 3c, e–h). Data described below indicate that S_T is a composite S2 + S3 fabric at this locality that envelops rims grown during two distinct tectonometamorphic events (M2–D2, M3–D3).

Chemical zoning in garnet porphyroblasts is complex (Figs 3e–h & 4a). Garnet cores (M1) have low Fe/(Fe + Mg) and X_{Grs} (0.85 and 0.03–0.05 respectively) and elevated X_{Sps} (up to 0.06), consistent with early growth zoning. Garnet tips (rims developed in S2 + S3 pressure shadows) have higher Fe/(Fe + Mg) and are low in Mn, except for extreme rims which have a 20-μm-wide high-Mn spike characteristic of retrograde garnet resorption (e.g. Kohn & Spear, 2000). Within the low-Mn tip of garnet no. 1 (Fig. 3e–g), there are two spikes in Ca, the inner one approximately 300 μm from the edge of the grain, and the outer one at the garnet rim. Within the inner Ca spike (interpreted to represent M2 garnet), Ca increases from X_{Grs} = 0.04–0.12 over a distance of 70 μm (Fig. 4a), with an abrupt change to low Ca (X_{Grs} = 0.03) immediately outboard of this spike. Ilmenite, apatite and one monazite inclusion that was analysed (see Monazite Geochronology) occur in this second low-Ca region assigned to M3 (Fig. 3g). The outer M3 spike in Ca is less abrupt, with Ca increasing from X_{Grs} = 0.04–0.10 over a distance of 180 μm. X-ray maps of other garnet porphyroblasts (e.g. Fig. 3h) indicate that these zoning patterns are a consistent feature of this sample and cannot be ascribed to disequilibrium processes (e.g. Carlson, 2002).

The prevalence of apatite, without monazite, allanite, or xenotime, as inclusions in garnet suggests that the abrupt increase in CaO within the inner (M2) spike may correspond to the first appearance of monazite, via a reaction involving apatite breakdown, such as:

© 2007 Blackwell Publishing Ltd

Table 2. (a) Garnet compositions used for thermobarometry; (b) mineral compositions used for thermobarometry.

	Sample – textural location[a]									
wt%	1-c	1-is	1-r	2-c	2-r	3-c	3-r	4-r	5-r	6-r
(a)										
SiO_2	36.88	37.02	37.41	36.38	36.23	37.16	37.54	36.72	37.48	38.51
Al_2O_3	20.91	21.08	21.12	20.43	20.51	21.04	21.38	20.93	21.37	21.62
FeO	36.32	34.58	34.52	39.46	39.41	28.81	31.84	36.55	25.08	27.13
MnO	1.59	0.73	1.51	1.17	1.28	1.67	3.01	0.95	7.22	2.89
MgO	2.98	2.75	2.58	1.45	1.50	1.44	2.74	3.02	3.39	4.08
CaO	1.51	4.09	3.41	0.40	0.75	9.30	2.78	0.99	5.93	6.59
	100.19	100.25	100.55	99.29	99.68	99.42	99.29	99.16	100.47	100.82
No. Ox.	12	12	12	12	12	12	12	12	12	12
Si	2.98	2.98	3.00	3.00	2.98	2.99	3.02	2.99	2.97	3.01
Al	1.99	2.00	1.99	1.99	1.99	2.00	2.03	2.01	2.00	1.99
Fe^{2+}	2.45	2.32	2.31	2.72	2.71	1.94	2.14	2.49	1.66	1.77
Mn	0.11	0.05	0.10	0.08	0.09	0.11	0.21	0.07	0.49	0.19
Mg	0.36	0.33	0.31	0.18	0.18	0.17	0.33	0.37	0.40	0.48
Ca	0.13	0.35	0.29	0.04	0.07	0.80	0.24	0.09	0.50	0.55
Total	8.02	8.03	8.01	8.01	8.02	8.01	7.97	8.01	8.03	7.99
X_{Fe}	0.87	0.88	0.88	0.94	0.94	0.92	0.87	0.87	0.81	0.79
X_{Grs}	0.04	0.12	0.10	0.01	0.02	0.26	0.08	0.03	0.17	0.18
X_{Sps}	0.04	0.02	0.03	0.03	0.03	0.04	0.07	0.02	0.16	0.06

	Sample – mineral											
	1-Ms	1-Bt	3-Bt	4-Bt	5-Hbl	6-Hbl	1-Pl	2-Pl	3-Pl	4-Pl	5-Pl	6-Pl
(b)												
SiO_2	45.33	35.70	36.13	36.11	44.78	44.47	66.90	63.98	60.90	66.31	63.82	61.60
TiO_2	0.51	2.02	2.53	2.09	0.51	0.41	0.00	0.00	0.00	0.00	0.00	0.00
Al_2O_3	36.67	18.90	20.05	19.12	12.52	14.86	20.10	22.12	24.00	20.45	22.09	24.32
FeO	1.16	20.07	18.01	20.53	16.69	14.55	0.10	0.00	0.34	0.03	0.30	0.01
MnO	nd	0.09	0.14	0.02	0.61	0.10	nd	nd	nd	nd	nd	nd
MgO	0.62	9.66	9.24	9.41	11.60	10.69	nd	nd	nd	nd	nd	nd
CaO	nd	nd	nd	nd	9.06	10.89	1.10	3.40	5.61	1.21	3.88	6.29
Na_2O	1.34	0.21	0.19	0.20	1.63	1.73	11.10	9.61	8.51	10.93	9.29	8.18
K_2O	9.92	9.13	9.25	8.81	0.41	0.31	0.02	0.10	0.10	0.11	0.09	0.03
F	0.30	0.09	0.05	0.15	nd	nd	nd	nd	nd	nd	nd	nd
Total	95.85	95.87	95.60	96.48	97.80	98.00	99.32	99.21	99.46	99.04	99.47	100.43
No. Ox.	11	11	11	11	23	23	8	8	8	8	8	8
Si	3.00	2.70	2.71	2.71	6.61	6.49	2.95	2.84	2.72	2.93	2.83	2.72
Ti	0.03	0.12	0.14	0.12	0.06	0.04	nd	nd	nd	nd	nd	nd
Al	2.86	1.69	1.77	1.69	2.18	2.56	1.04	1.16	1.27	1.07	1.16	1.27
Fe^{2+}	0.06	1.27	1.13	1.29	2.06	1.78	nd	nd	nd	nd	nd	nd
Mn	0.00	0.01	0.01	0.00	0.08	0.01	nd	nd	nd	nd	nd	nd
Mg	0.06	1.09	1.03	1.05	2.55	2.33	nd	nd	nd	nd	nd	nd
Ca	0.00	0.00	0.00	0.00	1.43	1.70	0.05	0.16	0.27	0.06	0.19	0.30
Na	0.17	0.03	0.03	0.03	0.47	0.49	0.95	0.83	0.74	0.94	0.80	0.70
K	0.84	0.88	0.89	0.84	0.08	0.06	0.00	0.01	0.01	0.01	0.01	0.00
F	0.06	0.02	0.01	0.04	0.00	0.00	0.00	0.00	0.00	0.00	0.00	0.00
Total	7.02	7.78	7.71	7.74	15.51	15.46	5.00	4.99	5.01	5.00	4.99	4.99
X_{Fe}	0.51	0.54	0.52	0.55	0.45	0.43						
X_{An}							0.05	0.16	0.27	0.06	0.19	0.30

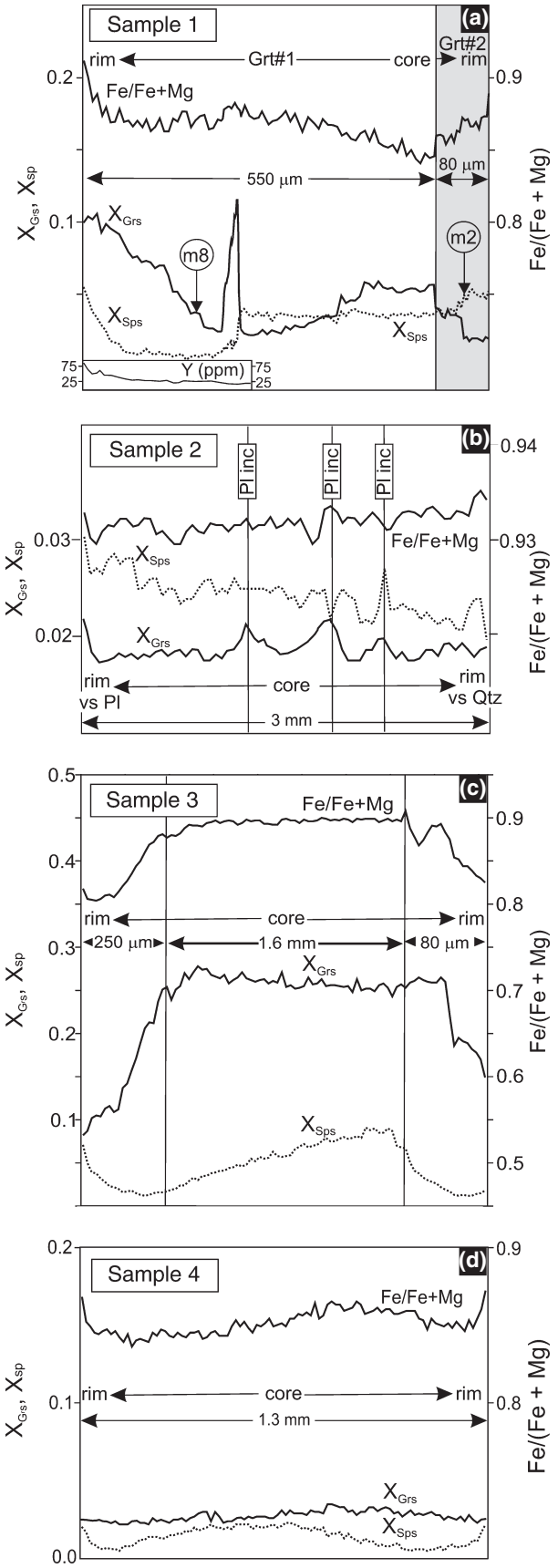
[a]c, core; is, inner spike; r,rim; nd, not determined/below detection limits.

$$\text{Chl} + \text{Qtz} + \text{Bt} + \text{Pl} + \text{Ap} = \text{Grt} + \text{Ms} + \text{Mnz} + \text{fluid} \quad (7)$$

The empirical relationship between bulk CaO/SiO_2 and monazite crystallization presented by Foster & Parrish (2003) yields 525 °C for the temperature of monazite appearance.

It is interesting to note that Y also increases at the extreme garnet rim, from 30 to 90 ppm over the outer ~80 μm of garnet no. 1. Rims enriched in Y are commonly interpreted as a retrograde feature, forming via garnet resorption and back-diffusion of Y into the porphyroblast (Pyle & Spear, 1999; Foster *et al.*, 2004). However, the preservation of high-Y annuli and Y growth zoning in upper amphibolite facies garnet with homogenous Mn profiles (e.g. Pyle & Spear, 1999; Foster *et al.*, 2004) suggest that the diffusivity of Y is lower than Mn in garnet. Given the greater width of the observed Y zoning (80 μm) compared with Mn zoning (20 μm), together with the limited development of retrograde biotite adjacent to the garnet rim (Fig. 3c), the rimward increase in Y is considered to reflect prograde garnet rim growth in equilibrium with matrix monazite, an interpretation quantified below using garnet–monazite thermometry.

© 2007 Blackwell Publishing Ltd



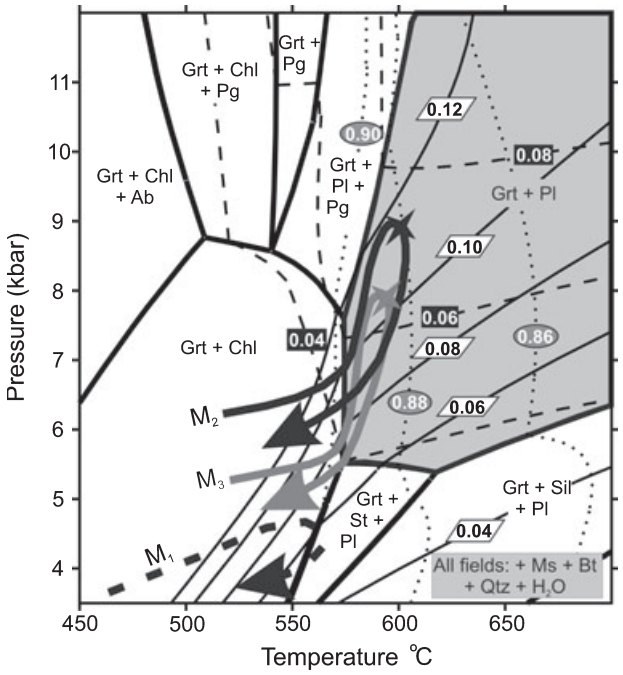


Fig. 5. Calculated phase diagram for sample 1 (some narrow fields not shown for clarity; melt field above ~650 °C not shown). Shaded area shows region of observed Grt-Bt-Ms-Pl-Qz assemblage. Note isopleths for garnet of X_{Grs} (thin solid curves), Fe/(Fe + Mg) (dotted curves), and modal fraction (dashed curves). Stars indicate estimated near-peak *P–T* values for M2 (black) and M3 (grey).

Matrix plagioclase is fairly uniform in composition ($X_{An} = 0.14$–0.19), with no variation related to distance from garnet porphyroblasts. Biotite compositions show minor but systematic variations that are consistent with slight Fe enrichment caused by a small amount of retrograde garnet resorption (Kohn & Spear, 2000). Biotite within ~0.2 mm of garnet and rims of grains up to 0.4 mm have higher Fe ($X_{Fe} = 0.56$) than cores of grains more than 0.4 mm from garnet ($X_{Fe} = 0.54$). M3 *P–T* conditions, calculated from the outer garnet rim (Table 2a, analysis 1-r) together with adjacent matrix plagioclase and low-Fe biotite, are 7.8 kbar and 595 °C.

The computed phase diagram for sample 1 (Fig. 5) is in good accord with thermobarometric results, with the observed chlorite- and staurolite-absent mineral assemblage constrained approximately to > 580 °C (chlorite breakdown) and > 6 kbar (Grt + St + Pl stability). Melt-producing reactions (not shown in Fig. 5) restrict maximum temperatures to less than ~650 °C. Calculated isopleths of X_{Grs} and Fe/(Fe + Mg) for the outer garnet rim (M3) composition [$X_{Grs} = 0.10$, Fe/(Fe + Mg) = 0.88] intersect at ~610 °C and 8 kbar. Based on the separation of X_{Grs}

Fig. 4. Compositional traverses of garnet in samples 1–4. Note location of monazite inclusions (M8 & M2) in (a). Vertical lines in (b) show location of plagioclase inclusions.

© 2007 Blackwell Publishing Ltd

isopleths (Fig. 5), the composition of the inner Ca spike [$X_{Grs} = 0.12$, Fe/(Fe + Mg) = 0.88; Table 2a, analysis 1-is] corresponds to M2 garnet growth at ~600 °C and 9 kbar.

It is important to note that the preservation of strong Mn zoning within this composite porphyroblast demonstrates that internal compositions have not been extensively modified by diffusive reequilibration. Importantly, the slope of calculated compositional modal isopleths dictate that garnet growth, together with increasing X_{Grs} and roughly constant Fe/(Fe + Mg), requires a quasi-isothermal pressure increase (Fig. 5). Thus the textural and chemical relationships suggest that, following M1 garnet core formation at low pressure (Fig. 5), the two garnet overgrowths reflect two metamorphic episodes (M2, M3) associated with tectonic loading. Geochronological data presented below are consistent with this suggestion.

Sample 2

Sample 2 is a kyanite-rich metasedimentary rock that was collected near the south flank of the large, Jurassic (Villeneuve *et al.*, 2003) Walhalla Creek pluton (Fig. 2). The sample is a coarse-grained Grt-Ky-St-Bt-Ms-Pl-Qtz-Ilm-Mt schist (Fig. 3d), with garnet up to 2 cm in diameter and coarse kyanite blades up to 5 cm long. Garnet, kyanite and staurolite generally overgrow the main (S2) foliation of the rock, with larger kyanite blades exhibiting some preferred alignment. Geochronology presented below indicates that these are M3 porphyroblasts. Kyanite is more abundant, adjacent to pods of leucogranite assumed to emanate from the pluton. The Al-rich, bulk-rock composition relative to other metapelitic rocks in this area, together with the coarse crystal size and proximity to the Walhalla Creek pluton, suggests that this sample underwent significant metasomatic changes during contact metamorphism.

The rock used for microprobe and SHRIMP analysis consists of ~80% kyanite that forms partially aligned blades up to 2 cm in length as well as shorter, randomly oriented grains. Inclusions of ilmenite and magnetite are generally unaligned. Garnet occurs as a single, 2 × 3 mm porphyroblast that contains small ilmenite inclusions defining a weak internal fabric parallel to the alignment of larger kyanite blades in the matrix. Staurolite forms subhedral to euhedral porphyroblasts, up to 1 mm in size, with abundant randomly oriented ilmenite and magnetite inclusions. Xenotime and monazite, up to 80 μm in long dimension, occur in the matrix as well as inclusions in kyanite, staurolite and garnet.

Compositional zoning in sample 2 is limited. Garnet porphyroblasts have uniform Fe/(Fe + Mg) of 0.93–0.94, X_{Sps} of 0.03 and X_{Grs} of 0.01–0.02, with higher X_{Grs} where garnet contacts matrix plagioclase and some plagioclase inclusions (Fig. 4b). Plagioclase is uniform in composition ($X_{An} = 0.04$–0.05).

The occurrence of sodic plagioclase and low-grossular garnet reduces the reliability of geobarometric results with equilibrium (1) (Todd, 1998). In addition, the absence of biotite prevents application of equilibrium (3), and the extremely low Mn content of ilmenite ($X_{sp} < 0.01$) compromises the retrieval of temperature estimates based on Mn-Fe exchange between garnet and ilmenite. A temperature of 600 °C was assumed, based on results for sample 1, and consistent with the calculated stability field of the Grt-St-Ky assemblage observed in sample 2. The compositions of the garnet rim and adjacent plagioclase lead to a calculated pressure of 7.6 kbar at 600 °C. The compositions of the garnet core and plagioclase inclusions in garnet yield 5.4 kbar at 600 °C.

Sample 3

Sample 3 is a Grt-Ky-St-Bt-Ms-Pl-Qtz schist collected in the north-eastern part of the study area (Fig. 2) from an outcrop with thin layers of Grt-amphibolite and sheets of generally concordant augen granite. These sheets are considered to emanate from the Mt Burnham augen granite because they increase in abundance approaching the main intrusive contact about 6 km to the west. The schist is also cross-cut by 5–50 cm thick sheets of undeformed, undated granite that in places is pegmatitic.

M2 garnet occurs as subhedral to strongly embayed grains generally < 2 mm in diameter which are enveloped by the external S2 fabric (Fig. 3i) defined by biotite, kyanite up to 3 cm in length, and elongate grains of feldspar, quartz and rare staurolite (Fig. 3i). Partial breakdown of kyanite and garnet is evident from ragged and embayed grains surrounded by biotite. Most garnet is inclusion-free, but some larger porphyroblasts have clear rims, with core regions (M1) containing internal quartz inclusion fabrics (assumed to represent S1). Post-M2–D2 staurolite also forms sparse, < 0.3 mm grains with sharp grain boundaries that cross-cut the foliation.

Garnet porphyroblasts are growth zoned with Ca-, Mn- and Fe-rich cores [$X_{Grs} = 0.25$–0.27; Fe/(Fe + Mg) = 0.93–0.95] compared with rims (Fig. 4c). Whereas garnet rims adjacent to quartz are moderately calcic ($X_{Grs} = 0.15$–0.16; Fe/(Fe + Mg) = 0.86–0.88), rims adjacent to plagioclase are significantly less calcic ($X_{Grs} = 0.083$–0.09; Fe/(Fe + Mg) = 0.86–0.87) but enriched in Mn (Fig. 4c), consistent with retrograde diffusional re-equilibration accompanying garnet resorption. Plagioclase varies fairly systematically in composition, from $X_{An} = 0.26$–0.28 within 100 μm of, or touching garnet, to $X_{An} = 0.19$–0.22 further away from garnet porphyroblasts. Similar to plagioclase, biotite shows small but systematic variations in composition. Further than ~200 μm from garnet, biotite has Fe/(Fe + Mg) = 0.51 with little variation between core and rims. Within 200 μm of garnet, biotite rims and cores have

© 2007 Blackwell Publishing Ltd

Fe/(Fe + Mg) = 0.53 and 0.52 respectively. The slight enrichment of biotite rims near garnet is interpreted to reflect retrograde garnet resorption during the latest metamorphic event, which also produced the most calcic plagioclase and least calcic garnet rims. Biotite and plagioclase compositions further away from garnet may have been in equilibrium with garnet during an early metamorphic event.

Given the pronounced growth zoning of garnet, reliable *P–T* conditions can only be calculated for garnet rims, touching plagioclase, and the core of nearby (within 50 μm) biotite. Relevant compositions (Table 2a,b) yield 6.1 kbar and 590 °C. These conditions, which were attained during M5 metamorphism (see Monazite Geochronology), represent maximum values, as the Mn enrichment of the garnet rim indicates resorption that probably caused some Fe enrichment of nearby biotite (e.g. Kohn & Spear, 2000).

Computed phase relationships for sample 3 (Fig. 6) afford a more complete picture of evolving *P–T* conditions. Isopleths of Fe/(Fe + Mg) and X_{Grs} that approximate the garnet core composition suggest M1 garnet growth (syn-D1) at ~9 kbar and 500 °C (shaded box in Fig. 6). The syn-S2 assemblage, Grt-Ky-Bt, is stable at ~9 kbar at temperatures between ~620 °C (chlorite-out; kyanite-in) and ~650 °C (melt-in; not shown in Fig. 6). The growth of post-S2 staurolite is consistent with the garnet rim *P–T* conditions.

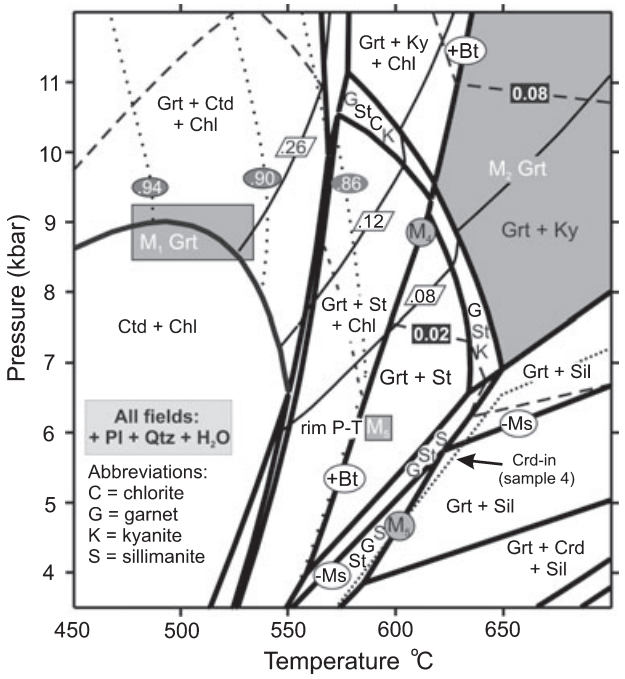


Fig. 6. Calculated phase diagram for sample 3 (some narrow fields not shown for clarity; melt field above ~650 °C not shown). Isopleths as in Fig. 5. Biotite is stable on the high-*T* side of curves labelled '+ Bt'. Muscovite is unstable on the high-*T* side of curves labelled '-Ms'. Shaded rectangle shows estimated *P–T* of garnet core growth (M1) based on calculated isopleths. Shaded grey region shows observed stability field of M2 assemblage. Grey square with white lettering shows maximum *P–T* of M5 event derived from sample 3 garnet rim compositions. Grey circle with black lettering at ~9 kbar shows M4 conditions derived from *P–T* results for sample 4. Grey circle with black lettering at low-*P* shows maximum pressure (at 600 °C) of cordierite stability calculated for sample 4 bulk composition.

Sample 4

Sample 4 was collected from an outcrop dominated by Grt-St-Ky-Bt-Ms-Pl-Qtz schist, ~5 km west of sample 3 and ~600 m east of the Mt Burnham augen granite (Fig. 2) in an area with more abundant sheets of augen granite than where sample 3 was collected. Coarse (0.5–3 cm) porphyroblasts of garnet, staurolite and kyanite overprint the foliation of the rock.

The thin section used for microprobe and SHRIMP analysis is staurolite-rich, with large staurolite porphyroblasts partially replaced by cordierite both internally and along rims (Fig. 3j). Longer crystals of post-M2 staurolite are subparallel to, but truncate the S2 foliation (Fig. 3j) which is defined by biotite and elongate plagioclase and quartz grains. Cordierite also occurs as irregular grains up to 1 mm in size that are interstitial to matrix plagioclase and quartz. M2 kyanite < 0.3 mm in length forms rare, ragged blades that are subparallel to the S2 foliation. Sparse, subhedral, post-M2 garnet porphyroblasts are < 0.2 mm in diameter and cut the S2 foliation.

Garnet porphyroblasts show slight growth zonation with small core to rim decreases in MnO, Fe/(Fe + Mg) and CaO (Fig. 4d). Garnet rims adjacent to plagioclase or biotite are enriched in Fe/(Fe + Mg) and MnO (Fig. 4d), consistent with retrograde garnet resorption. Plagioclase is uniform in composition (X_{An} = 0.06). Biotite shows systematic variations in composition. Further than ~400 μm from garnet, biotite has Fe/(Fe + Mg) = 0.55–0.56, whereas grains closer to garnet have higher Fe/(Fe + Mg) = 0.57–0.60.

Pressure–temperature conditions of 610 °C and 8.9 kbar were calculated from the composition of the least Fe-enriched biotite, adjacent plagioclase and the composition of garnet just inboard of the Mn-enriched rim. The computed stability field of the peak metamorphic assemblage (Grt-St-Ky) for sample 4, which is almost identical to that calculated for sample 3 (Fig. 6), is within 10 °C of these *P–T* conditions.

Geochronological data presented below suggest that these conditions were attained during M4 metamorphism. The slight rimward decrease in CaO in garnet may indicate garnet growth on a *P–T* path that is more shallow than computed isopleths of X_{Grs}. Alternatively, it may reflect re-equilibration during the M5 event, which is constrained to < 4.6 kbar at 600 °C (shaded circle in Fig. 6) by the calculated position of the breakdown of staurolite to cordierite.

© 2007 Blackwell Publishing Ltd

Garnet amphibolites (samples 5 & 6)

Two garnet amphibolite samples from the central and western parts of the region (Fig. 2) were analysed for the purpose of complementing thermobarometric data from metapelitic samples described above. Sample 5 was collected from a highly strained schist interlayered with high-strain granite sheets at the decimetre scale. Garnet porphyroblasts, which contain randomly oriented quartz and plagioclase inclusions, are enveloped by S2 defined primarily by amphibole and elongate grains of quartz and plagioclase. Sparse foliation-parallel biotite grains are weakly retrogressed to chlorite. Sample 6 is an amphibole-rich gneiss with hornblende up to 3 cm in length. Both garnet and amphibole contain an internal quartz inclusion fabric that are subparallel to the main foliation of the rock. Whereas the inclusion fabric within amphibole is generally parallel to the weak S2 imparted by moderately aligned amphibole, the internal fabric with garnet is at a high angle to S2.

Garnet porphyroblasts in sample 5 show only slight zonation, with a small rimward increase in CaO ($X_{Grs} = 0.13$–0.17), and constant Fe/(Fe + Mg) = 0.79–0.80 and MnO, except for extreme rims [Fe/(Fe + Mg) = 0.85]. Plagioclase is nearly constant in composition ($X_{An} = 0.23$–0.26), and hornblende also shows little compositional variation [Fe/(Fe + Mg) = 0.55–0.58]. Garnet porphyroblasts in sample 6 exhibit minor growth zonation, with a rimward decrease in CaO ($X_{Grs} = 0.21$–0.18) and Fe/(Fe + Mg) from 0.82 to 0.79. Plagioclase is fairly uniform in composition ($X_{An} = 0.37$–42). Hornblende that is not in contact with garnet ranges in Fe/(Fe + Mg) from 0.51 to 0.54.

Pressure–temperature results were derived from rim compositions. For sample 5, equilibria (4) and (5) yield 9.8 kbar and 615 °C. Equilibrium (6) yields 665 °C. For sample 6, equilibria (4) and (5) yield 9.5 kbar and 665 °C, with equilibria (5) and (6) recording the same temperature. In spite of the high temperatures, which appear unreasonable in comparison with the *P–T* results for, and the lack of evidence for melting of, metasedimentary rocks, the *P–T* results for both amphibolite samples confirm the high-*P* conditions retrieved from pelitic samples 1–4.

TIMS U-Pb GEOCHRONOLOGY

Sample 7 was collected from a sequence of interlayered amphibolite and calcsilicate along the Stewart River (Fig. 2). In this location, 15-cm- to 2-m-diameter boudins of calcsilicate are surrounded by more resistant 10–20 cm thick, fine- to medium-grained plagioclase-hornblende amphibolite. Titanite was separated from a sample of the mixed layer which commonly contains titanite. This titanite is interpreted to have formed during metamorphism, driven by the availability of Ca, Ti and Si within the mixed-layer package.

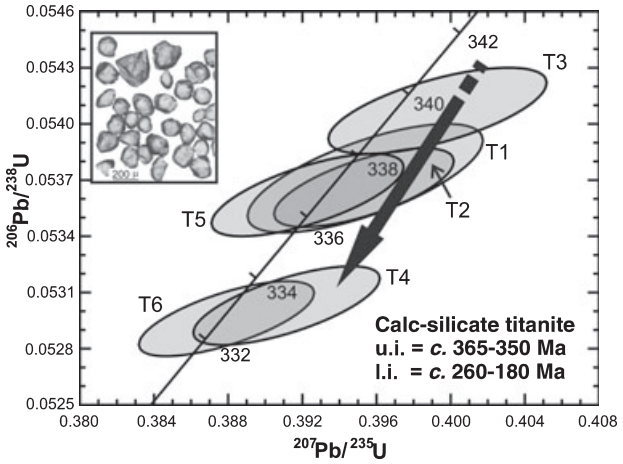


Fig. 7. Concordia plot showing titanite results for sample 7.

Titanite is pale brown to pale yellow, and sub-rounded to angular, without apparent core–overgrowth relationships (Fig. 7).

TIMS methodology is summarized in the Appendix. Multigrain fractions give near-concordant results (Fig. 7, Table 3) with two clusterings of data: a group of three fractions with a weighted average $^{206}Pb/^{238}U$ age of 336.9 ± 0.8 Ma (fractions T1, T2, T5) and a second with a similarly derived age of 332.9 ± 0.9 Ma (T4, T6). A single fraction gives a slightly older $^{206}Pb/^{238}U$ age of 339.5 ± 1.4 Ma. Because of the near-parallelism of the data array with the concordia curve, large uncertainties (> 100 Ma) are associated with the regressed upper and lower intercept ages of *c.* 367 and 266 Ma. Fixing a lower intercept of 260 Ma, a dominant age of plutonism in the area, results in an upper intercept age of 365 ± 40 Ma. Fixing a lower intercept of 180 Ma, the dominant ^{40}Ar-^{39}Ar cooling age for hornblende, an upper intercept of 350 ± 20 Ma results. Regardless of whether the titanite systematics reflect *c.* 260–180 Ma Pb loss or neocrystallization, the results thus point to initial titanite growth between *c.* 365 and 350 Ma.

MONAZITE GEOCHRONOLOGY

Details of the methodology for obtaining *in situ* analyses are described in the Appendix. Results are tabulated in Table 4. Interpretations are based on $^{206}Pb/^{238}U$ ages because the low abundance of ^{207}Pb in Phanerozoic monazite leads to not only imprecise, but potentially inaccurate $^{207}Pb/^{235}U$ ages which are strongly affected by the magnitude and choice of ^{204}Pb common-Pb correction. As such, concordia plots are not presented, although they may be generated from data in Table 4. The $^{206}Pb/^{238}U$ ages quoted in the text may slightly overestimate the actual age because of the well-known effect of disequilibrium uptake of ^{230}Th by monazite (Parrish, 1990). This effect decreases with age and is minimal to negligible in monazite older than

© 2007 Blackwell Publishing Ltd

Table 3. U-Pb TIMS analytical data for sample 7.

Fract.[a]	Description[b]	Wt. (μg)	U (ppm)	Pb[c] (ppm)	$^{206}Pb/^{204}Pb$[d]	Pb[e] (pg)	Isotopic ratios[f]							Ages (Ma)[h]						Disc. (%)
							$^{208}Pb/^{206}Pb$	$^{207}Pb/^{235}U$	± 1SE Abs	$^{206}Pb/^{238}U$	± 1SE Abs	Corr. coeff.[g]	$^{207}Pb/^{206}Pb$	± 1SE Abs	$^{206}Pb/^{238}U$	± 2SE	$^{207}Pb/^{235}U$	± 2SE	$^{207}Pb/^{206}Pb$	± 2SE	
T1 (53)	T,pBr,Alt,fIn,An,NAbr,M-0.75A	209	152	12	325	346	0.6	0.0537	0.0002	0.3954	0.0032	0.696	0.0534	0.0003	337.3	1.8	345.5	28.9	338.3	4.6	2.5
T2 (48)	T,pBr,Alt,fIn,An,NAbr,M-0.75A	256	154	12	330	422	0.59	0.0537	0.0001	0.3953	0.0024	0.671	0.0534	0.0003	337	1.3	347	22.6	338.2	3.5	3.0
T3 (40)	T,pY,Alt,fIn,An,Nabr,M-0.75A	283	164	13	333	496	0.59	0.0541	0.0001	0.3993	0.0029	0.651	0.0536	0.0003	339.5	1.4	352.4	27.8	341.1	4.3	3.8
T4 (58)	T,pY,Alt,fIn,An,Nabr,M-0.75A	150	125	9	314	209	0.59	0.053	0.0001	0.3879	0.0024	0.692	0.0531	0.0003	332.7	1.2	334.1	22	332.8	3.5	0.5
T5 (57)	T,pY,Alt,fIn,An,Nabr,M-0.75A	133	135	10	302	210	0.59	0.0536	0.0001	0.3923	0.0026	0.683	0.0531	0.0003	336.7	1.3	331.5	24.4	336	3.8	−1.6
T6 (48)	T,Co,Alt,fIn,An,NAbr,M-0.75A	119	142	10	301	197	0.57	0.053	0.0001	0.3912	0.0025	0.691	0.0535	0.0003	333.1	1.3	350	24	335.2	3.7	5.0

[a]Number in brackets refers to the number of grains in the analysis.
[b]Titanite descriptions: Co, colourless; pBr, pale brown; pY, pale yellow; fIn, few inclusions; An, anhedral; NAbr, not abraded; M-0.75, Magnetic at 0.75A 10 °SS.
[c]Radiogenic Pb.
[d]Measured ratio, corrected for spike and fractionation.
[e]Total common Pb in analysis corrected for fractionation and spike.
[f]Corrected for blank Pb and U and common Pb, errors quoted are 1-sigma absolute; procedural blank values for this study ranged from 0.1–0.2 pg U and 2–4 pg Pb for zircon analyses and 1–2 pg U and 8–9 pg Pb for titanite analyses; Pb blank isotopic composition is based on the analysis of procedural blanks; corrections for common Pb were made using Stacey–Kramers compositions.
[g]Correlation coefficient.
[h]Corrected for blank and common Pb, errors quoted are 2 sigma in Ma.

200 Ma (Heaman & Parrish, 1991). However, even in cases of extremely low Th/U in the monazite-growing fluid or melt, this effect should produce no more than 1–2 Myr excess in age. Errors are quoted at the 2-sigma level in the text and are statistical in nature.

Sample 1

Although monazite up to 20 μm in size is common in the matrix of sample 1, only two garnet porphyroblasts (garnet 1 & 2) host monazite inclusions near their rims (Figs 3g & 8a). These monazite, no. 8 and no. 2, form small (10 × 15 μm), partly rounded grains that show uniform Th, but one of which (no. 8; Fig. 3g) has a slightly Y-enriched rim (Fig. 8c). Single-spot analyses of each grain yield a weighted mean $^{206}Pb/^{238}U$ age of 239 ± 7 Ma [probability of fit (POF) = 57%; Table 4]. Matrix monazite forms equant (no. 22) to elongate (no. 20) grains interstitial to foliation-parallel biotite and muscovite grains. Grain 20 has a Y-rich rim, whereas grain 22 has uniformly higher Y (Fig. 8d, e). Spot analyses of each grain yield a weighted mean $^{206}Pb/^{238}U$ age of 187 ± 5 Ma (POF = 32%; Table 4).

Sample 2

Analyses of monazite were obtained for three inclusions in kyanite, two inclusions in garnet and one inclusion in staurolite. Monazite inclusions within kyanite and staurolite comprise euhedral to subhedral grains, >30 μm in shortest dimension and up to 80 μm in the longest dimension, and are variably intersected by very fine fractures that do not visibly transect host grains. X-ray maps of monazite grains reveal strong differences between grains. Monazite no. 71, within staurolite, is characterized by uniform Y concentrations, consistent with a single-age domain (Fig. 9a). In contrast, grain no. 74, within kyanite, exhibits complex variations in Y (Fig. 9b) which are mimicked by variations in Th, U and C. Monazite inclusions in garnet cores (no. 1, 6) show uniform Y except for Y-rich rims (Fig. 9c, d), which may reflect prograde breakdown of xenotime. Care was taken to avoid these Y-rich rims in the analysis of these grains (Fig. 9c, d). In spite of the textural and chemical differences described above, all seven analyses of these six monazite grains form a single population with a weighted mean $^{206}Pb/^{238}U$ age of 195.0 ± 1.7 Ma (POF = 53%; Table 4).

Sample 3

Monazite grains no. 8 and no. 2 are rounded, elongate, ~15 × 50 μm grains that occur within, and parallel to the foliation of this sample (Fig. 3i). Both grains show uniform, moderately high Y. Three spot analyses of these grains yield a weighted mean $^{206}Pb/^{238}U$ age of 114.3 ± 1.6 Ma (POF = 89%; Table 4).

© 2007 Blackwell Publishing Ltd

Table 4. SHRIMP U/Pb monazite results

Target	Texture	Y	Th/U	Pb* (ppm)	^{204}Pb (ppb)	^{204}Pb/^{206}Pb ± ^{204}Pb/^{206}Pb	f(206)^{204}	^{208*}Pb/^{206*}Pb ± ^{208}Pb/^{206}Pb	^{206*}Pb/^{238}U ± ^{206}Pb/^{238}U	^{207*}Pb/^{235}U ± ^{207}Pb/^{235}U	Corr. coeff.	^{207*}Pb/^{206*}Pb ± ^{207}Pb/^{206}Pb	Apparent ages (Ma)	
													^{206}Pb/^{238}U ± ^{206}Pb/^{238}U	^{207}Pb/^{235}U ± ^{207}Pb/^{235}U
Sample 1														
8509-2.1	Grt	lo	19.3	551	102	1.30E-03 ± 2.57E-04	0.024	6.1225 ± 0.0839	0.03849 ± 0.00134	0.23414 ± 0.0251	0.43933	0.04412 ± 0.00428	243.5 ± 8.4	213.6 ± 20.8
8509-8.1	Grt	lo-hi	12.4	678	129	9.08E-04 ± 1.32E-04	0.017	3.7492 ± 0.0381	0.03764 ± 0.00065	0.27187 ± 0.0132	0.46592	0.05238 ± 0.00227	238.2 ± 4.0	244.2 ± 10.6
8509-20.1	mat	m-hi	12.5	612	108	8.67E-04 ± 1.29E-04	0.016	3.9023 ± 0.0357	0.02972 ± 0.00053	0.19109 ± 0.0102	0.44563	0.04664 ± 0.00225	188.8 ± 3.3	177.6 ± 8.8
8509-22.1	mat	hi	16.9	633	371	3.49E-03 ± 6.43E-04	0.065	5.2509 ± 0.0885	0.02889 ± 0.00064	0.20864 ± 0.0431	0.22943	0.05237 ± 0.01061	183.6 ± 4.0	192.4 ± 36.9
Sample 2														
8506-73.1	Ky	hi	8.6	359	35	3.58E-04 ± 6.54E-05	0.007	2.5796 ± 0.0236	0.03130 ± 0.00042	0.20333 ± 0.0060	0.56120	0.04712 ± 0.00116	198.7 ± 2.7	187.9 ± 5.0
8506-71.1	St	hi	8.4	423	48	4.11E-04 ± 6.64E-05	0.008	2.5421 ± 0.0113	0.03103 ± 0.00036	0.19787 ± 0.0055	0.51931	0.04625 ± 0.00111	197.0 ± 2.3	183.3 ± 4.7
8506-6.1	Grt	lo-hi	6.7	282	18	2.07E-04 ± 6.21E-05	0.004	2.1033 ± 0.0114	0.03084 ± 0.00035	0.20785 ± 0.0058	0.51576	0.04888 ± 0.00118	195.8 ± 2.2	191.7 ± 4.9
8506-71.2	St	hi	8.5	472	28	2.15E-04 ± 1.61E-04	0.004	2.5933 ± 0.0206	0.03072 ± 0.00037	0.20542 ± 0.0116	0.32843	0.04850 ± 0.00260	195.1 ± 2.3	189.7 ± 9.7
8506-72.1	Ky	lo-hi	5.5	294	24	2.22E-04 ± 6.14E-05	0.004	1.6899 ± 0.0099	0.03062 ± 0.00037	0.20773 ± 0.0056	0.54818	0.04920 ± 0.00112	194.4 ± 2.3	191.6 ± 4.7
8506-1.1	Grt	lo-hi	7.0	326	31	3.04E-04 ± 8.29E-05	0.006	2.1367 ± 0.0115	0.03042 ± 0.00035	0.20066 ± 0.0068	0.44689	0.04784 ± 0.00146	193.2 ± 2.2	185.7 ± 5.7
8506-74.1	Ky	hi	2.3	328	30	1.65E-04 ± 4.27E-05	0.003	0.7284 ± 0.0044	0.03029 ± 0.00035	0.20676 ± 0.0041	0.66886	0.04951 ± 0.00074	192.4 ± 2.2	190.8 ± 3.4
Sample 3														
8508-2.1	mat	hi	8.5	324	63	7.14E-04 ± 9.45E-05	0.013	2.6429 ± 0.0184	0.01797 ± 0.00023	0.10786 ± 0.0045	0.42315	0.04353 ± 0.00166	114.8 ± 1.5	104.0 ± 4.1
8508-8.1	mat	hi	9.5	347	54	6.24E-04 ± 8.94E-05	0.012	2.9512 ± 0.0154	0.01790 ± 0.00021	0.11036 ± 0.0041	0.42269	0.04471 ± 0.00153	114.4 ± 1.3	106.3 ± 3.8
8508-8.2	mat	hi	7.7	320	155	1.62E-03 ± 1.44E-04	0.030	2.3762 ± 0.0168	0.01781 ± 0.00022	0.10648 ± 0.0062	0.32802	0.04336 ± 0.00242	113.8 ± 1.4	102.7 ± 5.7
Sample 4														
8507-11.1	St	l-m	5.3	437	57	3.42E-04 ± 5.45E-05	0.006	1.5798 ± 0.0067	0.02318 ± 0.00028	0.15455 ± 0.0037	0.59107	0.04836 ± 0.00094	147.8 ± 1.7	145.9 ± 3.3
8507-6.1	Crd/St	lo-m	7.7	606	100	5.65E-04 ± 5.76E-05	0.010	2.3796 ± 0.0177	0.02299 ± 0.00025	0.14964 ± 0.0047	0.45140	0.04721 ± 0.00134	146.5 ± 1.6	141.6 ± 4.2
8507-12.1	Crd/St	lo-m	8.0	643	112	6.06E-04 ± 8.59E-05	0.011	2.4489 ± 0.0123	0.02294 ± 0.00026	0.14826 ± 0.0050	0.44031	0.04687 ± 0.00143	146.2 ± 1.6	140.4 ± 4.4
8507-6.2	Crd/St	lo-m	11.3	492	77	7.02E-04 ± 8.30E-05	0.013	3.4759 ± 0.0139	0.02241 ± 0.00027	0.14078 ± 0.0049	0.45474	0.04556 ± 0.00143	142.9 ± 1.7	133.7 ± 4.4
8507-9.1	St	m-lo	12.2	421	55	6.31E-04 ± 8.60E-05	0.012	3.7606 ± 0.0159	0.02132 ± 0.00026	0.13115 ± 0.0048	0.44756	0.04461 ± 0.00148	136.0 ± 1.7	125.1 ± 4.3
8507-4.1	St	m-lo	10.7	438	47	4.69E-04 ± 8.83E-05	0.009	3.2757 ± 0.0210	0.02121 ± 0.00027	0.13286 ± 0.0057	0.40780	0.04543 ± 0.00178	135.3 ± 1.7	126.7 ± 5.1
8507-10.2	mat	m-lo	6.2	515	77	4.55E-04 ± 5.88E-05	0.008	1.9988 ± 0.0084	0.01948 ± 0.00021	0.12105 ± 0.0031	0.51176	0.04507 ± 0.00101	124.4 ± 1.3	116.0 ± 2.8
8507-9.2	St	m-hi	6.4	526	60	3.66E-04 ± 5.13E-05	0.007	2.1380 ± 0.0112	0.01839 ± 0.00021	0.11778 ± 0.0031	0.52734	0.04645 ± 0.00105	117.5 ± 1.3	113.1 ± 2.8
8507-10.1	mat	m	5.9	518	54	3.07E-04 ± 4.92E-05	0.006	1.9069 ± 0.0116	0.01816 ± 0.0002	0.11428 ± 0.0028	0.56399	0.04564 ± 0.00091	116.0 ± 1.3	109.9 ± 2.5
8507-17.2	mat	hi	4.0	539	63	2.71E-04 ± 3.63E-05	0.005	1.2701 ± 0.0064	0.01719 ± 0.00018	0.10926 ± 0.0023	0.60104	0.04610 ± 0.00078	109.9 ± 1.2	105.3 ± 2.1
8507-17.1	mat	hi	4.6	500	63	3.13E-04 ± 9.20E-05	0.006	1.4356 ± 0.0072	0.01673 ± 0.00019	0.10589 ± 0.0042	0.39799	0.04590 ± 0.00166	106.9 ± 1.2	102.2 ± 3.8

Texture: inclusions in Grt, St, Ky, Crd, Crd from breakdown of St (Crd/St); mat = matrix grain.
Y: relative concentration from X-ray map; lo = low, m = medium, hi = high; single values for homogenous grains; zoned grains show core–rim concentrations.
*Radiogenic Pb (corrected for common Pb).
^{207}Pb/^{235}U age is shown in grey as it is poorly constrained because of the low abundance of ^{207}Pb in young monazite.
Notes (see Stern, 1997): calibration standard 3345; Age 1821.0 Ma; 6/38 = 0.32642; Th/U calibration: F = 0.00000*UO + 0.85700.
Uncertainties reported at 1σ (absolute) and are calculated by numerical propagation of all known sources of error; error in 206Pb/238U calibration 1.0%.
f(206)^{204} refers to mole fraction of total ^{206}Pb that is due to common Pb, calculated using the ^{204}Pb-method; common Pb composition used is the surface blank (4/6: 0.05770; 7/6: 0.89500; 8/6: 2.13840).
IP347 (samples 2, 3, 4): Pb fractionation bias correction of 0.89% applied to ^{207}Pb/^{235}U age.
IP346 (sample 1): no Pb fractionation bias correction applied.

© 2007 Blackwell Publishing Ltd

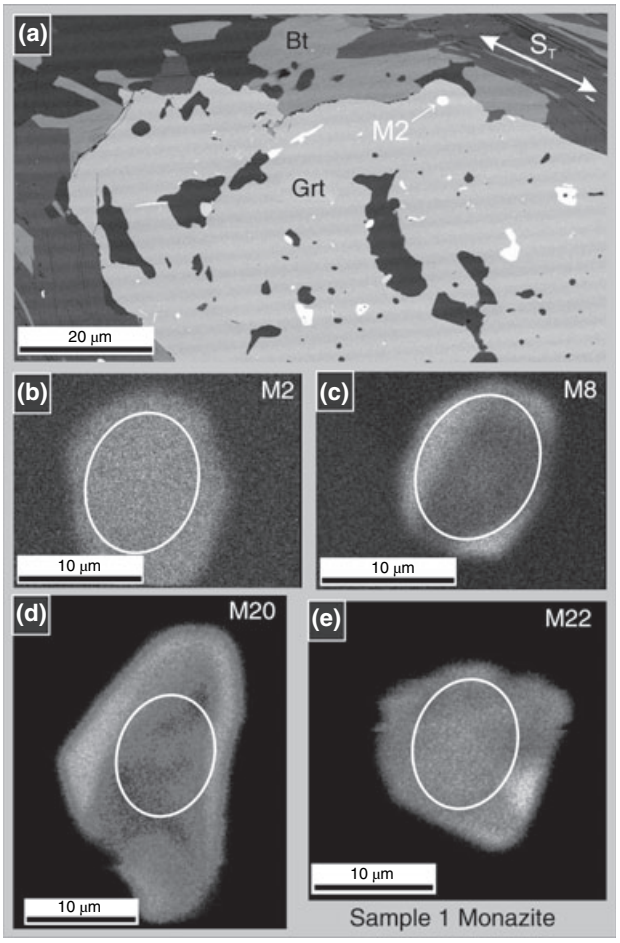


Fig. 8. Sample 1 images: (a) SEM backscattered image of garnet porphyroblast no. 2 showing location of monazite no. 2 near the low-Ca rim; (b–e) X-ray maps of Y in analysed monazite in sample 1. Brighter colours indicate higher concentration. Ellipses show location of SHRIMP analysis pits.

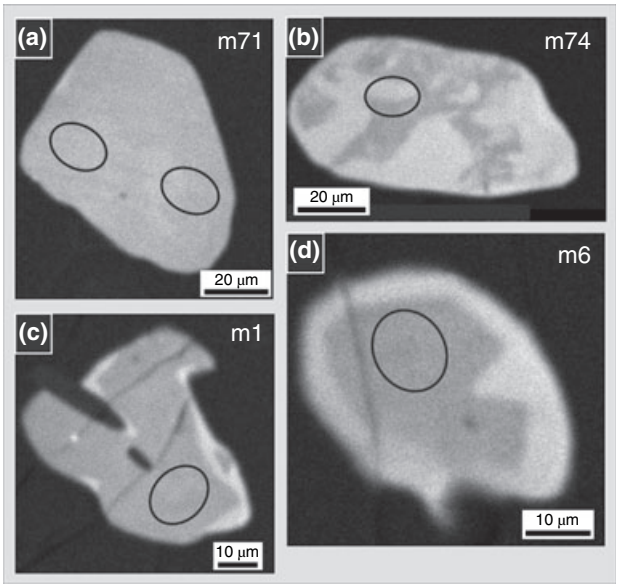


Fig. 9. X-ray maps of Y in analysed monazite in sample 2. Darker greys indicate higher concentration. Ellipses show location of SHRIMP analysis pits.

Sample 4

Seven monazite grains span a range of textural settings, display a variable amount of chemical zonation (Fig. 10), and yield a range of ages. Whereas all grains have at least thin, high-Y rims, grain 17 is the only grain that shows limited zoning and is uniformly high in Y. Two analyses of this euhedral matrix grain yield the youngest age for this sample, 108.4 ± 1.74 Ma (2σ internal errors; POF = 8%). Most other monazite grains are irregular in shape, and have discrete low-Y regions forming cores (nos 6, 10, 12; Fig. 10) or intermediate areas between moderate-Y cores and high-Y rims (no. 11; Fig. 10). The sharp boundaries between most of these zones suggest that they represent distinct stages of monazite growth (Williams *et al.*, 1999; Foster *et al.*, 2002; Gibson *et al.*, 2004). Four spot analyses of low-Y zones from three grains (nos 6, 11, 12) yield a statistically distinct population with a $^{206}Pb/^{238}U$ age of 146 ± 3 Ma (POF = 21%; Table 4). These grains are interpreted to represent primary inclusions in staurolite, with grains 6 and 12 touching staurolite, but occluded within cordierite that formed from staurolite breakdown (Fig. 3j). Given the tight clustering of these four analyses from similar, low-Y zones within three separate grains, the 146 ± 3 Ma age is interpreted as real, and not a product of partial reequilibration, recrystallization or mixing of older and younger monazite.

Analyses of grains 4, 9 and 10 are considered to represent composite ages as each analysis spot overlapped zones of different Y content (e.g. monazite nos 4 and 10 in Fig. 10). The youngest of these analyses (120 Ma; no. 10.1) comes from the rim of a euhedral

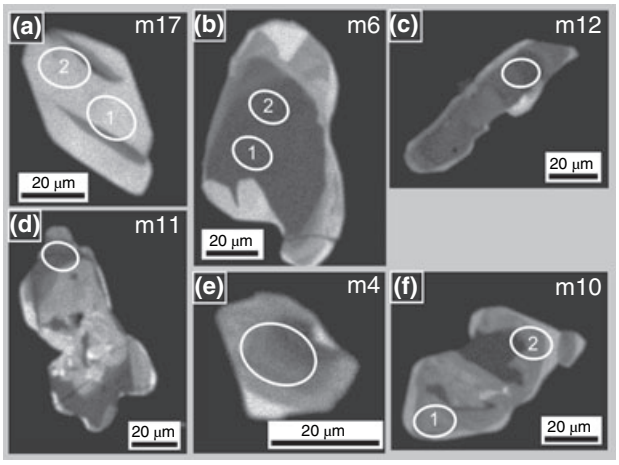


Fig. 10. X-ray maps of Y in analysed monazite in sample 4. Brighter colours indicate higher concentration. Ellipses show location of SHRIMP analysis pits.

© 2007 Blackwell Publishing Ltd

matrix grain which contains the smallest amount of low-Y monazite. In contrast to matrix grain 10, the chemical variations that characterize staurolite inclusions no. 4 and no. 9 are diffuse. This diffuse zoning is interpreted to reflect reequilibration induced by fluids introduced along fractures that transect these grains. Similar re-equilibration via fractures in host porphyroblasts has been documented in several other studies (e.g. Zhu *et al.*, 1997; Carson *et al.*, 2004).

INTERPRETATION OF METAMORPHIC AND GEOCHRONOLOGICAL DATA

In situ SHRIMP analyses of monazite in four metasedimentary rocks range in age from *c.* 239 to 107 Ma. Along with *c.* 365–350 Ma titanite in a calcsilicate, these data define five distinct metamorphic events (M1–M5). These results are discussed below in the context of the metamorphic history gleaned from observed textural relationships and quantitative analyses of each sample. In the subsequent Tectonic Implications section, our interpretations are compared with other available data that constrain the tectonic history of this portion of YTT. The following discussion is arranged in descending chronological order.

M1 event

Titanite in sample 7 is interpreted to have initially grown during a Devono-Mississippian (*c.* 365–350 Ma) metamorphic episode (M1), with new growth or Pb loss at either *c.* 260 or 180 Ma. In either case, the small amount of resetting of Devono-Mississippian titanite suggests that these rocks never subsequently attained temperatures above ~650 °C, a result consistent with the ~600 °C thermobarometric results obtained for other samples (Table 1). The texturally distinct cores of garnets in samples 1 and 3 (Fig. 3c,i) are considered to reflect a discrete period of deformation (D1) during the M1 event recorded by titanite in sample 7. The composition of these garnet cores suggest that M1 pressures increased from west (sample 1) to east (sample 3).

M2 event

Euhedral to slightly rounded monazite inclusions in two garnet porphyroblasts in sample 1 yield an average $^{206}Pb/^{238}U$ age of *c.* 239 Ma for the M2 metamorphic event. Given the high closure temperature of monazite (Cherniak *et al.*, 2004), the uniform chemistry of the cores of these grains, and the absence of fractures that might have brought fluids into contact with them (e.g. Zhu *et al.*, 1997; Carson *et al.*, 2004), it is unlikely that these grains have partially reset ages. In comparison with this 239 Ma monazite age, U-Pb analysis of low Th/U overgrowths on detrital zircon grains of the mica schist indicate metamorphism at *c.* 260 ± 3 Ma (Villeneuve *et al.*, 2003). Taken at face value, the younger age of monazite determined here suggests that M2 metamorphism extended from *c.* 260 to 239 Ma, somewhat longer than the presently known duration of plutonism between *c.* 260 and 253 Ma.

The conservative interpretation of accessory mineral inclusions is that they yield the maximum age of a host porphyroblast and enveloping fabric (e.g. DeWolf *et al.*, 1993; Zhu *et al.*, 1997; Foster *et al.*, 2002; Berman *et al.*, 2005). Additional textural and/or chemical characteristics are required to substantiate interpretation of inclusions as synmetamorphic and/or syntectonic. For example, the distribution of monazite inclusions can constrain the timing of monazite growth relative to various porphyroblasts (Pyle & Spear, 1999, 2003; Foster *et al.*, 2002, 2004) or to specific metamorphic reactions (Pyle & Spear, 2003; Kohn & Malloy, 2004; Berman *et al.*, 2005). The zoning of Y has been effectively used to determine the relative timing of monazite and garnet growth (Pyle & Spear, 1999, 2003; Foster *et al.*, 2002, 2004; Gibson *et al.*, 2004; Kohn & Malloy, 2004). As the only significant reservoirs of Y are xenotime and garnet (Bea, 1996; Bea & Montero, 1999), changes in the proportion of garnet (via crystallization or resorption) dramatically affect the Y content of a rock's effective bulk composition and hence the Y content of crystallizing monazite. However, for polymetamorphic rocks with more complex reaction histories, Y zoning alone may not provide sufficient information to link the growth of specific monazite grains or zones to specific porphyroblasts or zones of porphyroblasts (e.g. Carson *et al.*, 2004; Berman *et al.*, 2005). Recent advances in accessory mineral thermometry were used to test and support textural interpretations regarding which garnet zones were in equilibrium with dated monazites. Specifically, the *P–T* derived from thermobarometry and phase relationships is compared with temperatures calculated from the Pyle *et al.* (2001) calibration of the equilibrium:

$$\mathrm{YAG} + \mathrm{Ap} + \mathrm{Qtz} = \tfrac{5}{4}\mathrm{Grs} + \tfrac{5}{4}\mathrm{An} + 3\mathrm{Y\text{-}mnz} + \tfrac{1}{2}\mathrm{H_2O} \quad (8)$$

where YAG and Y-mnz are Y component of garnet and monazite respectively.

In sample 1, garnet porphyroblasts display two high-Ca spikes within syntectonic rims. The occurrence of monazite no. 8 just outside the inner Ca spike within garnet no. 1 (Fig. 3g) is interpreted to result from monazite crystallization in the rock matrix just outboard of, and synchronously (in equilibrium) with, this inner zone of high-Ca garnet. Support for this correlation is derived from the congruence between the calculated monazite-garnet temperature (615 °C; Table 5) and the near-peak temperature estimated from silicate equilibria (600 °C; Table 1). A significantly lower monazite-garnet temperature (540 °C) is derived from pairing monazite no. 8 with the adjacent

© 2007 Blackwell Publishing Ltd

Table 5. Monazite-garnet temperatures calculated for sample 1 with equilibrium (8).

		Mineral compositions								
Mnz	Grt zone	X_Y(Mnz)	X_Y(Grt)	X_{Grs}	X_{An}	X_{OH}(Ap)	P	f_{H_2O}	ln K	T
m8	Inner hi-Ca spike (M_2)	0.0032	0.00004	0.12	0.17	0.26	8	7100	9.036	615
	Adjacent low-Ca (M_3)	0.0032	0.00006	0.04	0.17	0.26	8	5700	3.315	540
m2	Adjacent low-Ca (M_2)	0.0054	0.00014	0.04	0.17	0.15	4	1800	2.333	535
m22	Low-Ca M3 tip	0.0189	0.00006	0.03	0.17	0.15	8	7000	8.217	600
m22	Mid-Ca M3 tip	0.0189	0.00010	0.06	0.17	0.15	8	7500	9.318	620
m22	High-Ca M3 tip	0.0189	0.00016	0.10	0.17	0.15	8	7300	9.734	625
m20	High-Ca M3 tip	0.0090	0.00016	0.10	0.17	0.15	8	7000	7.487	590

low-Ca garnet, which is continuously zoned to the outer high-Ca rim and is interpreted to have been in equilibrium with the Jurassic (M3) matrix monazite (see M3 event below). The high-Y rim of monazite no. 8 may reflect post-peak-M2 garnet resorption. Monazite no. 2 and the adjacent, outer part of the low-Ca core (M2) of garnet 2 (Fig. 8a) yield a monazite-garnet temperature of 530 °C. This result is in excellent agreement with the temperature of monazite appearance predicted empirically. It also indicates earlier (lower-T) crystallization of monazite no. 2 during prograde M2 garnet growth (Fig. 5), consistent with the higher Y content of monazite no. 2 *v.* no. 8 (Table 5).

The first high-Ca overgrowth and accompanying high strain transposition deformation (D2) are thus inferred to be Late Permian in age. As discussed above, calculated phase relationships for sample 1 indicate that the growth of the inner high-Ca garnet resulted from a near isothermal pressure increase up to ~9 kbar at 600 °C. However, the occurrence of monazite no. 2 within the low-Ca portion of one garnet porphyroblast demonstrates that some monazite growth was initiated at low pressure.

M3 event

The single, 195 ± 1.9 Ma age population of monazite inclusions in garnet and kyanite porphyroblasts of sample 2 marks a Jurassic metamorphic event (M3), with peak P–T conditions of ~7.6 kbar and 600 °C. All signs of the M1 and M2 events in sample 2 are interpreted to have been destroyed by metasomatism that produced the anomalously aluminous bulk composition of this sample during the Jurassic (*c.* 202 Ma; M. Villeneuve, unpublished data) intrusion of the Walhalla Creek Pluton.

In sample 1, analyses of two small matrix grains that occur in the interstices of matrix biotite indicate M3 crystallization at *c.* 187 Ma, ~60 Myr younger than M2 monazite inclusions in garnet porphyroblasts of this sample. The 187 Ma matrix monazite is correlated with crystallization of the outer tip of garnet no. 1, which is zoned from low to high Ca, with the latter recording P–T conditions of 7.8 kbar and 595 °C. Two observations support this correlation. First, these P–T results based on silicate equilibria are in good agreement with calculated monazite-garnet temperatures for matrix monazite (no. 22) and the progression of compositions from the low-Ca, low-Y inner part (600 °C) to the high-Ca, high-Y rim (625 °C) of the outer tip of garnet no. 1 (Table 5). On the other hand, much lower temperatures (520–530 °C) result from pairing these garnet compositions with monazite no. 8 that occurs within this garnet tip. Second, the Jurassic metamorphism dated in sample 2 yields P–T conditions very similar to the conditions estimated from the outer rim of garnet no. 1. In addition, both samples record evidence for increasing pressure during garnet growth. For sample 2, thermobarometric results suggest that pressure increased from ~5.4 to 7.6 kbar. For sample 1, calculated phase relations (Fig. 5) indicate that the zoning from low to high CaO observed in the outer garnet overgrowth (Figs 3g & 4a) can only accompany garnet growth with increasing pressure.

The high Y content of matrix monazite has generally been ascribed to crystallization either in the presence of xenotime, which buffers Y to high values, or during or after garnet breakdown, which increases the Y content of the effective bulk composition, sometimes to the point of xenotime crystallization (Pyle & Spear, 1999, 2003; Foster *et al.*, 2002, 2004; Gibson *et al.*, 2004). The only xenotime that occurs in sample 1 are several small (< 15 μm) grains interstitial to matrix biotite and muscovite, but always within 30 μm of strongly resorbed, low-Ca garnet far removed from porphyroblasts that show garnet overgrowths. Xenotime is thought to have formed during the retrograde portion of the M2 metamorphic event via a garnet breakdown (and release of Y) reaction such as:

$$\text{Grt} + \text{Ms} + \text{Ap} = \text{Bt} + \text{Pl} + \text{Qtz} + \text{xenotime}$$

The presence of xenotime during subsequent growth of matrix monazite during M3 would have buffered the Y content to high values such as that observed in monazite no. 22 (7210 ppm). Consumption of xenotime during prograde growth of M3 garnet tips, would decrease the Y content of the effective bulk composition such that later matrix monazite would contain lower Y, as observed in the rims of matrix monazite no. 20 (3520 ppm). The slightly lower monazite-garnet temperature (Table 5) derived from monazite no. 20 (590 °C) compared with monazite no. 22 (625 °C), suggests that its growth occurred on the retrograde

© 2007 Blackwell Publishing Ltd

path that produced the slight garnet resorption inferred from garnet rims with higher Mn.

It is considered unlikely that the slightly younger age of matrix monazite in sample 1 (187 ± 5 Ma), compared with monazite in sample 2 (195 ± 2 Ma), results from analysing a small portion of monazite rims that re-equilibrated or grew during younger (Cretaceous) events discussed below, because matrix grain no. 22 has a single growth zone of uniform composition (Fig. 8e), and coeval ^{40}Ar-^{39}Ar hornblende cooling ages for hornblende rule out younger thermal events in this region (Villeneuve *et al*., 2003). Instead, the results are interpreted to indicate diachronous monazite crystallization during the *c*. 195–187 Ma, M3 metamorphic event.

M4 and M5 events

Samples 3 and 4 in the Mt Burnham area (Fig. 2) record Cretaceous monazite ages from 146 to 107 Ma (Tables 1 and 4) which are interpreted to define two distinct metamorphic events (M4 & M5). The youngest interstitial monazite in sample 4 (*c*. 107 Ma) is similar in age to elongate matrix monazite in sample 3 (*c*. 114 Ma). Although these results do not comprise a single statistical population, they are very similar to the 111.0 ± 0.2 Ma age of monazite previously reported from the Mount Burnham orthogneiss (Mortensen, 1990).

The youngest textural and chemical features of samples 3 and 4 are interpreted to correlate with the *c*. 110 Ma monazite in these samples. In sample 3, low-Ca rims of garnet constrain the pressure of M5 to have been <6.1 kbar, and textural and chemical evidence for garnet resorption correlates well with the uniformly high Y content of the matrix monazite analysed (Fig. 3i inset). *P–T* conditions of <4.6 kbar at 600 °C are indicated by the partial breakdown of staurolite to cordierite in sample 4 (Fig. 6), and the high Y content of 107 Ma monazite also suggests garnet breakdown.

The 146 Ma average age of monazite interpreted to represent primary inclusions in staurolite (grains 6 & 12 occur in cordierite formed from staurolite breakdown) yields a maximum age of staurolite growth in sample 4. As calculated phase relations for this sample indicate staurolite + garnet + kyanite stability (without chlorite) at pressures more than ~7 kbar, it is likely that staurolite grew during the high-*P* (~9 kbar) M4 event at *c*. 146 Ma rather than at a later time (e.g. 110 Ma) characterized by low-*P* metamorphism and garnet breakdown. Furthermore, the low Y content of *c*. 146 Ma monazite (e.g. Fig. 10b) also suggests that this monazite grew while garnet was stable, not breaking down at lower pressure.

TECTONIC IMPLICATIONS

Although it has been speculated for some time that YTT from Alaska to northern British Columbia has experienced a long, punctuated tectonic evolution based on age dating of its constituent magmatic rocks (Mortensen, 1990, 1992; Colpron *et al*., 2006a), our study is the first major mapping project to employ tools to discern the metamorphic conditions and deformational history that accompanied the magmatic pulses. The Middle Palaeozoic magmatic evolution of YTT has recently been subdivided into six magmatic cycles: I – Ecstall (390–365 Ma); II – Finlayson (365–357 Ma); III – Wolverine (357–342 Ma); IV – Little Salmon (342–314 Ma); V – Klinkit (314–269 Ma); and VI – Klondike (269–253 Ma), named after the regions they are best represented in Nelson *et al*. (2006) and Piercey *et al*. (2006). The Stewart River area hosts arc-related igneous rocks that are associated with three of these cycles: the Finlayson, Wolverine and Klondike. The new data reported here record evidence for multiple ages of amphibolite facies metamorphism and deformation that broadly coincide with these magmatic events.

Figure 11 summarizes through a series of schematic time slices the tectonic evolution of YTT as deciphered through our findings in the Stewart River geology. The proposed evolution builds heavily on four decades of research in YTT that are well summarized in Colpron *et al*. (2006a,b).

Devonian to Mississippian (M1–D1 event)

A growing body of evidence indicates that an arc developed on a siliciclastic substrate (the Snowcap assemblage) of the thinned, western continental margin of North America in the Late Devonian (at *c*. 375 Ma) in Alaska (Colpron *et al*., 2006a; Dusel-Bacon *et al*., 2006), and was in full bloom by about 365–360 Ma, when a large belt of porphyritic alkali-feldspar granite to monzogranite was intruded along much of its length (Mortensen, 1992; Piercey *et al*., 2006; Ruks *et al*., 2006). This arc formed in response to initiation of east-dipping subduction (Fig. 11a) of older, cold oceanic crust of the Late Proterozoic to Early Palaeozoic proto-Pacific Ocean floor. As this arc matured, its back-arc area rifted to form a widening ocean basin (Slide Mountain Ocean) during the Finlayson magmatic cycle. At this stage, the outboard portion of YTT almost certainly rifted free of North America (see Nelson *et al*., 2006 and references therein).

Our data do not distinguish whether the M1–D1 event was concurrent with the Finlayson (365–357 Ma) magmatic cycle, or with the widespread monzogranite that characterized the 347–342 Ma phase (Wolverine cycle) of arc magmatism (Piercey *et al*., 2006; Ruks *et al*., 2006) that intruded the Stewart River area. Deformation and exhumation of the Stewart River area during the latter time is suggested by the presence of 345 Ma detrital zircon within siliciclastic rocks (Villeneuve *et al*., 2003). Colpron *et al*. (2006b) also inferred deformation at 345–342 Ma and a Mississippian unconformity below the Pelmac Quartzite in the Glenlyon area.

© 2007 Blackwell Publishing Ltd

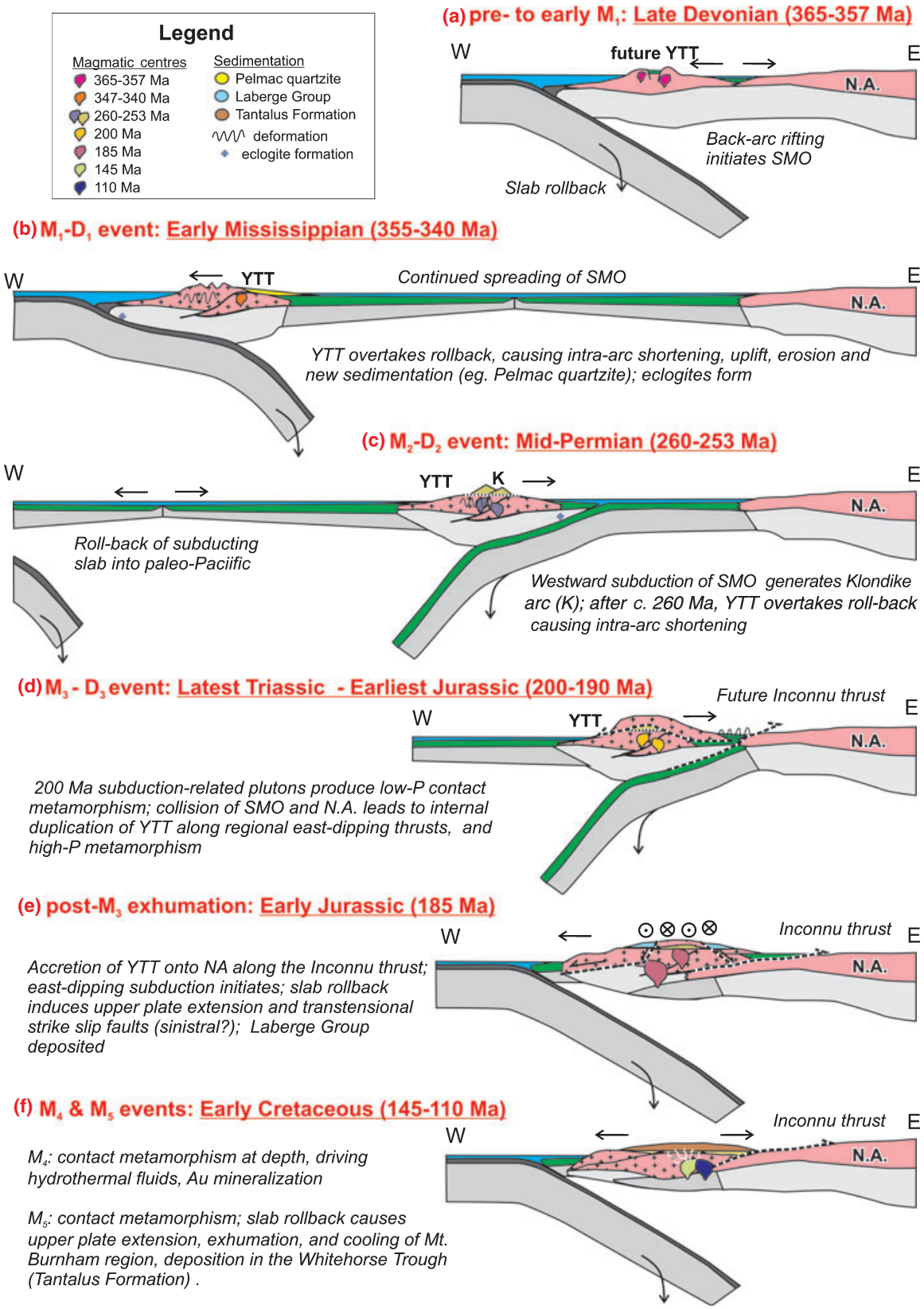


Fig. 11. Tectonic cartoon for the Devonian to Cretaceous evolution of the Stewart River area in YTT (see text for discussion).

© 2007 Blackwell Publishing Ltd

Deformation, metamorphism and exhumation are considered to have occurred within the active arc, when westward migration of YTT relative to North America overtook subduction rollback at *c.* 350 Ma. This caused intra-arc shortening, with internal deformation, thickening, uplift, erosion and new sedimentation (e.g. Pelmac quartzite; Fig. 11b). Preservation of Early Mississippian (*c.* 353 Ma) eclogites within YTT (Erdmer *et al.*, 1998; Devine *et al.*, 2006) may also point to a change in the dynamics of the active subduction zone.

Permian (M2–D2 event)

A major phase of Permian magmatism, the Klondike magmatic cycle of Piercey *et al.* (2006), is predominantly *c.* 260 Ma, but spans *c.* 265–253 Ma in age (Villeneuve *et al.*, 2003; Breitsprecher & Mortensen, 2004; Ruks *et al.*, 2006). This event is represented by metavolcanic rocks (the Klondike schist) and a suite of K-feldspar-porphyritic granites which are thought to reflect the initiation of west-dipping subduction of SMO underneath YTT (Fig. 11c; see also Nelson *et al.*, 2006; Piercey *et al.*, 2006).

The age of fabric development in the Permian plutons and the Klondike schist has been difficult to establish. Mortensen (1990) speculated that fabric development was Jurassic based on K-Ar ages in muscovite in syntaxial veins within the Klondike schist. However, our data indicate that the Permian, not the Jurassic, was the most important period of deformation. The Jim Creek pluton (Fig. 2) intruded late syntectonically, cutting across the transposition foliation while dykes of the pluton record a weak K-feldspar stretching lineation. The Jim Creek pluton has yielded multiple Permian ages (Breitsprecher & Mortensen, 2004), indicating that fabric development was pre-254 Ma, and post-260 Ma. The conclusion that Permian metamorphism (M2) was synchronous with deformation (D2) accords with the occurrence in sample 1 of Permian garnet overgrowths in D2 pressure shadows (Fig. 3c, e–h).

Our new *P–T* data indicate that the Permian (M2) metamorphic event initiated at low pressure, consistent with a synmagmatic origin, and culminated with growth of garnet at high pressure (~9 kbar). Support for a regional high-*P* event at this time comes from high-*P* amphibolite facies metamorphism in southern YTT (Stevens, 1996) and in YTT in Alaska, where ^{40}Ar-^{39}Ar ages are 260 to 215 Ma (Dusel-Bacon *et al.*, 2002). Detailed structural work in the Finlayson Lake region, once contiguous with the Stewart River area prior to offset along the Tintina Fault (Fig. 1), points to a major period of north-east-vergent thrust imbrication in the Early Permian (Murphy *et al.*, 2006).

The onset of the Permian event in YTT is marked by *c.* 270 Ma, ~15 kbar eclogites (Creaser *et al.*, 1997; Erdmer *et al.*, 1998) which probably formed during subduction of SMO (Mortensen, 1992). An intra-oceanic setting for YTT (Fig. 11c) is consistent with a relatively wide Slide Mountain Ocean and the lack of any effects of this deformation on the ancestral North American margin. Thus the M2–D2 event in YTT is suggested to represent a period of intra-arc thickening, which was induced by migration of YTT towards North America and accommodated by spreading in the Pacific Ocean.

Late Triassic–Early Jurassic (M3–D3 event)

Abundant Late Triassic to Early Jurassic plutons in Yukon (e.g. Mortensen, 1992; Dusel-Bacon *et al.*, 2002; Villeneuve *et al.*, 2003) are considered to reflect continued west-dipping subduction just prior to closure of Slide Mountain Ocean (Fig. 11d). Although rapid exhumation following plutonism has been documented for YTT (e.g. Johnston *et al.*, 1996; Dusel-Bacon *et al.*, 2002), our new data indicate that, prior to unroofing, the Jurassic represented a significant period of tectonic burial, with M3 garnet growth in samples 1 and 2 while pressure increased from ~5.4 to 7.8 kbar. Support for Jurassic regional tectonic loading also comes from the Minto area, ~120 km south-east of the Stewart River area (Fig. 1), where TIMS U-Pb geochronological data are interpreted to indicate low-*P* metamorphism, tectonic burial, deformation and mineralization, followed by rapid exhumation, all between *c.* 198 ± 2 and 195 ± 1 Ma (Tafti & Mortensen, 2004). This regional loading event is thought to reflect collision of YTT with North America (Fig. 11d).

Given the inferred collisional event, it is interesting that our data suggest that the main D2 transposition foliation is Permian, not Jurassic in age. The Jurassic was not a time of major fabric formation in the Stewart River region, because the S_T transposition foliation in Permian and older rocks are cut by a Jurassic dyke (M. Villeneuve, unpublished U-Pb data) that is only weakly folded itself, and undeformed dykes of the Jurassic Walhalla Creek pluton also cut the foliation. Moreover, the Permian Jim Creek pluton is unfoliated and older Permian plutons are highly strained. Consistent with these constraints, randomly oriented kyanite in sample 2 attests to a largely static Jurassic metamorphism. Thus growth of Jurassic garnet rims in D2 pressure shadows in sample 1 appears to reflect local fabric reactivation during heterogeneously distributed strain that was strongly partitioned into regional high-strain zones. This scenario is consistent with evidence for Jurassic thrusting in YTT in Alaska (Dusel-Bacon *et al.*, 2002) and in the Finlayson Lake area, where YTT is separated from North American strata by the regional, terrane bounding, Inconnu thrust, which is thought to have initiated in the Jurassic (Murphy *et al.*, 2006). Because no regional Jurassic faults have been identified in the Stewart River area, Jurassic tectonic loading of this area (Fig. 11d) is interpreted to have been accommodated along a major structural

© 2007 Blackwell Publishing Ltd

break(s) outside (structurally above) the area. One possibility is that the Finlayson Lake area (back-arc) was loaded onto the Stewart River area (main arc axis) by movement on the Teslin Fault (Fig. 1), an east-dipping thrust of probable Jurassic age (Colpron *et al.*, 2003; Snyder *et al.*, 2005; White *et al.*, 2006).

Our geochronological data indicate 195 ± 2 Ma prograde M3 metamorphism with increasing pressure, consistent with initiation of this event during emplacement of *c.* 200 Ma subduction-related plutons and subsequent tectonic loading (Fig. 11d). Retrograde resorption of garnet occurred during crystallization of high-Y, matrix monazite at 187 ± 5 Ma (sample 2). Early Jurassic ^{40}Ar-^{39}Ar cooling ages (*c.* 185–175 Ma) for hornblende, muscovite and biotite across most of the Stewart River area (Villeneuve *et al.*, 2003) and adjacent YTT in Alaska (Dusel-Bacon *et al.*, 2002) implicate significant Jurassic exhumation (Fig. 11e). However, the implied cooling rate of ~10–20 °C Myr^{-1} is not sufficiently well linked to changing crustal levels, nor are *P–T–t* paths sufficiently well constrained, to distinguish whether exhumation was accomplished via thrusting (as suggested by Dusel-Bacon *et al.*, 2002), extensional faulting, or erosion (e.g. see discussion by Ring *et al.*, 1999). Our preferred model (Fig. 11e) involves transtension (sinistral) during slab rollback after the onset of east-dipping subduction in the Early Jurassic.

Cretaceous (M4–M5 events)

A conspicuous feature of available ^{40}Ar-^{39}Ar data (Villeneuve *et al.*, 2003) is the anomalously young, Cretaceous ages in the north-eastern area around Mt Burnham (Fig. 2). Similarly, whereas our *in situ* dating of samples 1 and 2 revealed no monazite younger than Jurassic, samples 3 and 4 from the Mt Burnham area record discrete metamorphic events at *c.* 146 (M4) and 114–107 Ma (M5).

The 146 ± 3 Ma monazite in sample 4 is similar to *c.* 145–141 Ma ^{39}Ar-^{40}Ar ages of white mica (Breitsprecher & Mortensen, 2004; M. Villeneuve & C. Hart, unpublished data, 2006) from auriferous, mesothermal quartz veins in the Klondike schist (Mortensen *et al.*, 1992), and strengthens the case for a discrete thermal event (M4) at this time. The apparently restricted aerial extent of *c.* 146 Ma metamorphism raises the possibility that this event represents a hitherto unrecognized episode of plutonism related to east-dipping subduction beneath YTT (Fig. 11f). This magmatism could have induced contact metamorphism at depth in the Mt Burnham region, and fuelled Au-bearing hydrothermal fluids and greenschist facies retrogression at higher structural levels within the Klondike schist.

The *c.* 114–107 Ma matrix monazite is interpreted to have grown during a low-*P* metamorphic overprint (M5) experienced by both samples. These ages overlap with U-Pb monazite and zircon ages compiled by Breitsprecher & Mortensen (2004) for granitoid plutons dated in YTT in Alaska (108 Ma) and in the Finlayson Lake region (114–110 Ma), which was adjacent to the Mt Burnham area prior to Cretaceous–Tertiary offset along the Tintina Fault. The ages of these granitoids, which form part of a ~250 km-wide belt of *c.* 110–85 Ma granite plutons across the northern Cordillera, suggest that monazite growth in samples 3 and 4 was a contact metamorphic effect. Although no Cretaceous crystallization ages have yet been determined in the Mt Burnham area, there are abundant granite to monzonite dykes, as yet undated, suggestive of a nearby unroofed pluton.

In contrast to the rest of the Stewart River region which by 175 Ma had already cooled through biotite closure after significant (5–10 km) exhumation, the Mt Burnham region was at a deep structural level (~9 kbar) at 146 Ma. Exhumation of the Mt Burnham region to ~4.5 kbar is thought to have taken place during post-146 Ma regional extension that was caused by slab rollback (Fig. 11f). This late differential exhumation of the Mt Burnham region suggests that an extensional fault may separate it from the rest of the Stewart River area, although extant geophysical data do not show any obvious discontinuity in this region of poor outcrop. The textural contrast between elongate, foliation-parallel, 114 Ma monazite in sample 3 (Fig. 3i) and equant 107 Ma monazite in sample 4 (Fig. 10a) may indicate that extensional deformation was ongoing at 114 Ma and ceased by 107 Ma. This scenario offers some support for the *c.* 130–110 Ma extensional unroofing proposed for parts of YTT in adjacent regions of Alaska (Dusel-Bacon *et al.*, 2002) and the Finlayson Lake area (Murphy, 2004).

CONCLUSIONS

The Stewart River area hosts Devonian to Permian rocks that are the most thoroughly deformed and metamorphosed at a regional scale in YTT. The success in this study of linking *in situ* SHRIMP geochronology with quantitative metamorphic conditions has revealed one of the most complex polymetamorphic histories recorded at any one location in the Cordillera. These results demonstrate that the region has undergone at least three tectonometamorphic events between 365 and 180 Ma that are commensurate with regional magmatic events recorded in YTT (e.g. Piercey *et al.*, 2006), as well as two Cretaceous metamorphic events. In addition, the discovery of a *c.* 146 Ma thermal event in the Mt Burnham area lends credence to ^{40}Ar-^{39}Ar ages for gold vein emplacement in the Klondike at that time, the potential source of its world-famous placer gold deposits, and suggests that the Early Cretaceous may have been a more important magmatic and mineralizing event than generally recognized.

Our study demonstrates very distinct styles of deformation and metamorphism between the early and late phases of YTT's tectonic evolution. The most obvious high-strain deformation events (D1 and D2)

© 2007 Blackwell Publishing Ltd

occurred during the Devonian to Permian, within intra-oceanic magmatic arc environments while YTT was separated from North America by Slide Mountain Ocean. The Jurassic to Cretaceous metamorphic history recorded here is considered to be associated with accretion of YTT to North America, wherein metamorphic events accompanied magmatic pulses, but deformation was accommodated more along regional faults than by penetrative internal strain.

ACKNOWLEDGEMENTS

Many people have added valuable field work and/or discussions to the project; most notably M. Colpron, P. Glombick, D. Murphy, S. Piercey, C. Roots and T. Ruks. N. Rayner and K. Venance provided exceptional help with analytical data and M. Jercinovic provided high-quality X-ray maps of monazite. M. Colpron provided a very thoughtful review of an early draft. Constructive reviews by D. Gibson, J. Jones and D. Murphy are gratefully acknowledged. This is Geological Survey of Canada contribution no. 20060517, funded as part of the Northern Resources Development Program.

REFERENCES

Aranovich, L. Ya., 1991. *Mineral Equilibria of Multicomponent Solid Solutions*. Nauka Press, Moscow.

Bea, F., 1996. Residence of REE, Y, Th and U in granites and crustal protoliths; implications for the chemistry of crustal melts. *Journal of Petrology*, **37,** 521–552.

Bea, F. & Montero, P., 1999. Behavior of accessory phases and redistribution of Zr, REE, Y, Th, and U during metamorphism and partial melting of metapelites in the lower crust; an example from the Kinzigite Formation of Ivrea-Verbano, NW Italy. *Geochimica et Cosmochimica Acta*, **63,** 1133–1153.

Berman, R. G., 1990. Mixing properties of Ca-Mg-Fe-Mn garnets. *American Mineralogist*, **75,** 328–344.

Berman, R. G., 1991. Thermobarometry using multi-equilibrium calculations: a new technique, with petrological applications. *Canadian Mineralogist*, **29,** 833–855.

Berman, R., Sanborn-Barrie, M., Stern, R. & Carson, C., 2005. Tectonometamorphism at *c*. 2.35 and 1.85 Ga in the Rae domain, western Churchill Province, Nunavut, Canada: insights from structural, metamorphic and *in situ* geochronological analysis of the southwestern Committee Bay belt. *Canadian Mineralogist*, **43,** 409–442.

Breitsprecher, K. & Mortensen, J.K., 2004. *YukonAge 2004: A database of isotopic age determinations for rock units from Yukon Territory (release 3.0); Yukon Geological Survey, CD-ROM*. Canadian Geochronology Knowledgebase, 2006, http://gdr.ess.nrcan.gc.ca/geochron/e/explorer.htm, Geoscience Data Repository, Geological Survey of Canada, Earth Sciences Sector, Natural Resources Canada, Government of Canada.

de Capitani, C., 1994. Gleichgewichts-Phasendiagramme:Theorie und Software. *Berichte der Deutschen Mineralogischen Gesellschaft, Beihefte zum European Journal of Mineralogy*, **6,** 48.

Carlson, W. D., 2002. Scales of disequilibrium and rates of equilibration during metamorphism. *American Mineralogist*, **87,** 185–204.

Carson, C. J., Berman, R. G., Stern, R. A., Sanborn-Barrie, M., Skulski, T. & Sandeman, H. A. I., 2004. Age constraints on the Paleoproterozoic tectonometamorphic history of the Committee Bay region, western Churchill Province, Canada: evidence from zircon and *in situ* monazite SHRIMP geochronology. *Canadian Journal of Earth Sciences*, **41,** 1049–1076.

Chatterjee, N. D. & Froese, E., 1975. A thermodynamic study of the pseudobinary join muscovite-paragonite in the system $KAlSi_3O_8$–$NaAlSi_3O_8$-Al_2O_3-SiO_2-H_2O. *American Mineralogist*, **60,** 985–993.

Cherniak, D. J., Watson, E. B., Grove, M. & Harrison, T. M., 2004. Pb diffusion in monazite; a combined RBS/SIMS study. *Geochimica et Cosmochimica Acta*, **68,** 829–840.

Colpron, M., Murphy, D.C., Nelson, J. L. *et al*. 2003. Yukon Targeted Geoscience Initiative, Part 1: Results of accelerated bedrock mapping in Glenlyon (105L/1–7, 11–14) and northeast Carmacks (115I/9,16) areas, central Yukon. In: *Yukon Exploration and Geology 2002* (eds Emond, D.S. & Lewis, L.L.), pp. 85–108. Exploration and Geological Services Division, Yukon Region, Indian and Northern Affairs Canada, Whitehorse, Yukon.

Colpron, M., Nelson, J. L. & Murphy, D. C., 2006a. A tectonostratigraphic framework for the pericratonic terranes of the northern Cordillera. In: *Paleozoic Evolution and Metallogeny of Pericratonic Terranes at the Ancient Pacific Margin of North America, Canadian and Alaskan Cordillera, Special Paper 45* (eds Colpron, M. & Nelson, J.L.), pp. 1–23. Geological Association of Canada, St. Johns, Newfoundland.

Colpron, M., Mortensen, J. K., Gehrels, G. E. & Villeneuve, M. E., 2006b. Basement complex, Carboniferous magmatism and Paleozoic deformation in Yukon-Tanana terrane of central Yukon: field, geochemical and geochronological constraints from Glenlyon map-area. In: *Paleozoic Evolution and Metallogeny of Pericratonic Terranes at the Ancient Pacific Margin of North America, Canadian and Alaskan Cordillera, Special Paper 45* (eds Colpron, M. & Nelson, J.L.), pp. 131–151. Geological Association of Canada, St. Johns, Newfoundland.

Creaser, R. A., Heaman, L. M. & Erdmer, P., 1997. Timing of high-pressure metamorphism in the Yukon-Tanana terrane, Canadian Cordillera: constraints from U-Pb zircon dating of eclogite from the Teslin tectonic zone. *Canadian Journal of Earth Sciences*, **34,** 709–715.

Devine, F., Carr, S. D., Murphy, D. C., Davis, W. J. & Villeneuve, M., 2006. Geochronological and geochemical constraints on the origin of the Klatsa metamorphic complex: implications for Early Mississippian high-pressure metamorphism within Yukon-Tanana terrane. In: *Paleozoic Evolution and Metallogeny of Pericratonic Terranes at the Ancient Pacific Margin of North America, Canadian and Alaskan Cordillera, Special Paper 45* (eds Colpron, M. & Nelson, J.L.), pp. 107–130. Geological Association of Canada, St. Johns, Newfoundland.

DeWolf, C. P., Belshaw, N. S. & O'Nions, R. K., 1993. A metamorphic history from micron-scale $^{207}Pb/^{206}Pb$ chronometry of Archean monazite. *Earth and Planetary Science Letters*, **120,** 207–220.

Dover, J.H., 1994. Geology of part of east-central Alaska. In: *The Geology of Alaska. The Decade of North American Geology*, Volume G-1 (eds Plafker, G. & Berg, H.C.), pp. 153–204. Geological Society of America, Boulder, Colorado.

Dusel-Bacon, C. & Hansen, V.L., 1992. High-pressure amphibolite-facies metamorphism and deformation within the Yukon-Tanana and Taylor Mountain terranes, eastern Alaska. In: *Geologic Studies in Alaska by the U.S. Geological Survey, 1991, Bulletin 2041* (eds Bradley, D.C. & Dusel-Bacon, C.), pp. 140–159. U.S. Geological Survey, Washington, D.C.

Dusel-Bacon, C., Hansen, V. L. & Scala, J. A., 1995. High-pressure amphibolite facies dynamic metamorphism and the Mesozoic tectonic evolution of an ancient continental margin, east-central Alaska. *Journal of Metamorphic Geology*, **15,** 9–24.

© 2007 Blackwell Publishing Ltd

Dusel-Bacon, C., Lanphere, M. A., Sharp, W. D., Layer, P. W. & Hanson, V. L., 2002. Mesozoic thermal history and timing of structural events for the Yukon-Tanana Upland, east-central Alaska: $^{40}Ar/^{39}Ar$ data from metamorphic and plutonic rocks. *Canadian Journal of Earth Sciences*, **39,** 1013–1051.

Dusel-Bacon, C., Hopkins, M. J., Mortensen, J. K., Dashevsky, S., Bressler, J. R. & Day, W. C., 2006. Paleozoic tectonic and metallogenic evolution of the pericratonic rocks of east-central Alaska and adjacent Yukon. In: *Paleozoic Evolution and Metallogeny of Pericratonic Terranes at the Ancient Pacific Margin of North America, Canadian and Alaskan Cordillera, Special Paper 45* (eds Colpron, M. & Nelson, J.L.), pp. 25–74. Geological Association of Canada, St. Johns, Newfoundland.

Erdmer, P., Ghent, E. D., Archibald, D. A. & Stout, M. Z., 1998. Paleozoic and Mesozoic high-pressure metamorphism at the margin of ancestral North America in central Yukon. *Geological Society of America Bulletin*, **110,** 615–629.

Fallas, K.M., Erdmer, P., Creaser, R.A., Archibald, D.A. & Heaman, L.M., 1999. New terrane interpretation for the St. Cyr klippe, south-central Yukon. In: *Slave-Northern Cordillera Lithospheric Evolution (SNORCLE) Transect and Cordilleran Tectonic Workshop Meeting* (eds Cook, F. & Erdmer, P.), pp. 130–137. Lithoprobe Report No. 69, Univeristy of Calgory, Calgary, Alberta.

Foster, G. & Parrish, R. R., 2003. Metamorphic monazite and the generation of *P-T*-t paths. In: *Geological Society Special Publications 220* (eds Vance, D., Muller, W. & Villa, I.M.), pp. 25–47. Geological Society, London.

Foster, G., Gibson, H. D., Parrish, R., Horstwood, M., Fraser, J. & Tindle, A., 2002. Textural, chemical and isotopic insights into the nature and behaviour of metamorphic monazite. *Chemical Geology*, **191,** 183–207.

Foster, G., Parrish, R. R., Horstwood, M. S. A., Chenery, S., Pyle, J. & Gibson, H. D., 2004. The generation of prograde *P-T*-t points and paths; a textural, compositional, and chronological study of metamorphic monazite. *Earth and Planetary Science Letters*, **228,** 125–142.

Fuhrman, M. L. & Lindsley, D. H., 1988. Ternary-feldspar modeling and thermometry. *The American Mineralogist*, **73,** 201–216.

Gabrielse, H., Murphy, D.C. & Mortensen, J.K., 2006. Cretaceous and Cenozoic dextral orogen-parallel displacements, magmatism and paleogeography, north-central Canadian Cordillera. In: *Paleogeography of the North American Cordillera: evidence for Major Lateral Displacements in the North American Cordillera, Special Paper 46* (eds Haggart, J.W., Enkin, R.J. & Monger, J.W.H.). pp. 255–276, Geological Association of Canada, St. Johns, Newfoundland.

Gibson, H. D., Carr, S. D., Brown, R. L. & Hamilton, M. A., 2004. Correlations between chemical and age domains in monazite,and metamorphic reactions involving major pelitic phases: an integration of ID-TIMS and SHRIMP geochronology with Y–Th–U X-ray mapping. *Chemical Geology*, **211,** 237–260.

Gordey, S. P. & Ryan, J. J., 2005. *Geology, Stewart River area (115N, 115-O and part of 115J), Yukon Territory*. Geological Survey of Canada, Open File 4970 (1 sheet, 1:250 000 scale).

Heaman, L. & Parrish, R.R., 1991. U-Pb geochronology of accessory minerals. *Mineralogical Association of Canada Short Course Handbook*, **19,** 59–102.

Holland, T. J. B. & Blundy, J. D., 1994. Non-ideal interactions in calcic amphiboles and their bearing on amphibole-plagioclase thermometry. *Contributions to Mineralogy and Petrology*, **116,** 433–447.

Holland, T. J. B. & Powell, R., 1998. An internally consistent thermodynamic data set for phases of petrological interest. *Journal of Metamorphic Geology*, **16,** 309–343.

Johnston, S. T., Mortensen, J. K. & Erdmer, P., 1996. Igneous and metaigneous age constraints for the Aishihik metamorphic suite, southwest Yukon. *Canadian Journal of Earth Sciences*, **33,** 1543–1555.

Kohn, M. J. & Malloy, M. A., 2004. Formation of monazite via prograde metamorphic reactions among common silicates: implications for age determinations. *Geochimica et Cosmochimica Acta*, **68,** 101–113.

Kohn, M. J. & Spear, F., 2000. Retrograde net transfer reaction insurance for pressure-temperature estimates. *Geology*, **28,** 1127–1130.

Kretz, R., 1983. Symbols for rock-forming minerals. *American Mineralogist*, **68,** 277–279.

Ludwig, K. R., 2001. *User's Manual for Isoplot/Ex rev. 2.49: A Geochronological Toolkit for Microsoft Excel*. Special Publication 1a, Berkeley Geochronology Center, Berkeley, CA, pp. 55.

Mader, U. K., Percival, J. A. & Berman, R. G., 1994. Thermobarometry of garnet-clinopyroxene-hornblende granulites from the Kapuskasing structural zone. *Canadian Journal of Earth Sciences*, **31,** 1134–1145.

McMullin, D. W. A., Berman, R. G. & Greenwood, H. J., 1991. Calibration of the SGAM thermobarometer for pelitic rocks using data from phase-equilibrium experiments and natural assemblages. *Canadian Mineralogist*, **29,** 889–908.

Mortensen, J. K., 1990. Geology and U-Pb geochronology of the Klondike district, west-central Yukon. *Canadian Journal of Earth Sciences*, **27,** 903–914.

Mortensen, J. K., 1992. Pre-mid-Mesozoic tectonic evolution of the Yukon-Tanana terrane, Yukon and Alaska. *Tectonics*, **11,** 836–853.

Mortensen, J. K., Nesbitt, B. E & Rushton, R., 1992. Preliminary observations on the geology and geochemistry of quartz veins in the Klondike district,west-central Yukon. In: *Yukon Geology*, Volume 3 (ed. Brenner, T. J.), pp. 260–270, Indian and Northern Affairs Canada, Whitehorse, Yukon.

Murphy, D.C., 2004. Devonian-Mississippian metavolcanic stratigraphy, massive sulphide potential and structural reinterpretation of Yukon-Tanana terrane south of the Finlayson Lake massive sulphide district, southeastern Yukon (105G/1, 105H/3,4,5). In: *Yukon Exploration and Geology 2003* (eds Emond, D.S. & Lewis, L.L.), pp. 157–175. Exploration and Geological Services Division, Indian and Northern Affairs Canada, Whitehorse, Yukon.

Murphy, D.C., Mortensen, J.K., Piercey, S.J., Orchard, M.J. & Gehrels, G.E., 2006. Mid-Paleozoic to early Mesozoic tectonostratigraphic evolution of Yukon-Tanana and Slide Mountain terranes and affiliated overlap assemblages, Finlayson Lake massive sulphide district, southeastern Yukon. In: *Paleozoic Evolution and Metallogeny of Pericratonic Terranes at the Ancient Pacific Margin of North America,Canadian and Alaskan Cordillera, Special Paper, 45* (eds Colpron, M. & Nelson, J. L.), pp. 75–105. Geological Association of Canada, St. Johns, Newfoundland.

Nelson, J.L., Colpron, M., Piercey, S.J., Dusel-Bacon, C., Murphy, D.C. & Roots, C.F., 2006. Paleozoic tectonic and metallogenic evolution of the pericratonic terranes in Yukon, northern British Columbia and eastern Alaska. In *Paleozoic Evolution and Metallogeny of Pericratonic Terranes at the Ancient Pacific Margin of North America,Canadian and Alaskan Cordillera, Special Paper 45* (eds Colpron, M. & Nelson, J. L.), pp. 323–360. Geological Association of Canada, St. Johns, Newfoundland.

Parrish, R. R., 1990. U-Pb dating of monazite and its application to geological processes. *Canadian Journal of Earth Sciences*, **27,** 1431–1450.

Parrish, R. R., Roddick, J. C., Loveridge, W. D. & Sullivan, R. W., 1987. Uranium-lead analytical techniques at the geochronology laboratory, Geological Survey of Canada. *Radiogenic Age and Isotope Studies: Report 1*. Geological Survey of Canada, Paper 87-2, 3–7.

Perchuk, A. Phillipot, P., Erdmer, P. & Fialin, M., 1999, Rates of thermal equilibration at the onset of subduction deduced from diffusion modeling of eclogitic garnets, Yukon-Tanana terrane, Canada. *Geology*, **27,** 531–534.

© 2007 Blackwell Publishing Ltd

Piercey, S. J., Nelson, J. L., Colpron, M., Dusel-Bacon, C., Roots, C. F. & Simard, R.-L., 2006. Paleozoic magmatism and crustal recycling along the ancient Pacific margin of North America, northern Cordillera. In: *Paleozoic Evolution and Metallogeny of Pericratonic Terranes at the Ancient Pacific Margin of North America, Canadian and Alaskan Cordillera, Special Paper 45* (eds Colpron, M. and Nelson, J.L.), pp. 281–322. Geological Association of Canada, St. Johns, Newfoundland.

Pouchou, J. L. & Pichoir, F., 1985. PAP correction procedure for improved microanalysis. In: *Microbeam Analysis* (ed Armstrong, J.T.), pp. 104–106. San Francisco Press, San Francisco, CA.

Pyle, J. M. & Spear, F. S., 1999. Yttrium zoning in garnet; coupling of major and accessory phases during metamorphic reactions. *The American Mineralogist*, **88,** 708.

Pyle, J. M. & Spear, F. S., 2003. Four generations of accessory-phase growth in low-pressure migmatites from SW New Hampshire. *The American Mineralogist*, **88,** 338–351.

Pyle, J. M., Spear, F. S., Rudnick, R. L. & McDonough, W. F., 2001. Monazite–xenotime–garnet equilibrium in metapelites and a new monazite–garnet thermometer. *Journal of Petrology*, **42,** 2083–2107.

Rayner, N. & Stern, R. A., 2002. *Improved Sample Preparation Method for SHRIMP Analysis of Delicate Mineral Grains Exposed in Thin Sections*. Current Research of the Geological Survey of Canada, 2002-F10, 1–3.

Ring, U., Brandon, M. T., Willett, S. D. & Lister, G. S., 1999. Exhumation processes. *Geological Society Special Publications*, **154,** 1–27.

Roddick, J. C., 1987. Generalized numerical error analysis with applications to geochronology and thermodynamics. *Geochimica and Cosmochimica Acta*, **51,** 2129–2135.

Ruks, T. W., Piercey, S. J., Ryan, J. J., Villeneuve, M. E. & Creaser, R. A., 2006. Mid- to Late Paleozoic K-Feldspar Augen Granitoids of the Yukon-Tanana Terrane, Yukon, Canada: Implications for Crustal Growth and Tectonic Evolution of the Northern Cordillera. *Geological Society of America Bulletin*, **118,** 1212–1231.

Ryan, J. J. & Gordey, S. P., 2001. *New Geological Mapping in Yukon-Tanana Terrane near Thistle Creek, Stewart River Map Area, Yukon Territory*. Current Research of the Geological Survey of Canada, 2001-A2, 24.

Ryan, J. J. & Gordey, S. P., 2002. *Bedrock Geology of the Yukon-Tanana Terrane, Southern Stewart River Map Area, Yukon Territory*. Current Research of the Geological Survey of Canada, 2002-A2, 11.

Ryan, J. J., Gordey, S. P., Glombick, P., Piercey, S. J. & Villeneuve, M. E., 2003. *Update on Bedrock Geological Mapping of the Yukon-Tanana Terrane, Southern Stewart River Map Area, Yukon Territory*. Current Research of the Geological Survey of Canada, 2003-A9, 7.

Snyder, D. B., Roberts, B .J. & Gordey, S. P. 2005, Contrasting seismic characteristics of three major faults in northwestern Canada. *Canadian Journal of Earth Sciences*, **42,** 1223–1237

Stern, R. A., 1997. The GSC sensitive high resolution ion microphobe (SHRIMP): analytical techniques of zircon U-Th-Pb age determinations and performance evaluation. *Radiogenic Age and Isotopic Studies: Report 10*. Geological Survey of Canada, Current Research 1997-F, 1–31.

Stern, R. A. & Berman, R. G., 2000. Monazite U-Pb and Th-Pb geochronology by ion microprobe, with an application to in situ dating of an Archean metasedimentary rock. *Chemical Geology*, **172,** 113–130.

Stevens, R. A., 1996. Dorsey assemblage: pre-mid-Permian high temperature and pressure metamorphic rocks in the Dorsey Range, south Yukon Territory. In: *Slave-Northern Cordillera Lithospheric Evolution (SNORCLE) Transect and Cordilleran Tectonic Workshop Meeting* (eds Cook, F. & Erdmer, P.), Lithoprobe Report No. 50, pp. 70–75. University of Calgary, Calgary, Alberta.

Tafti, R. & Mortensen, J. K., 2004. Deformed Early Jurassic Porphyry Cu(-Au) Deposits at Minto and Williams Creek, Carmacks Copper Belt, Western Yukon Territory. Geological Society of America, Abstracts with Programs, 36, 516.

Tempelman-Kluit, D. J., 1979. Transported cataclasite, ophiolite and granodiorite in Yukon: Evidence of arc-continent collision. *Geological Survey of Canada*, **79–14,** 27.

Tinkham, D. K., Zuluaga, C. A. & Stowell, H. H., 2001. Metapelite phase equilibria modeling in MnNCKFMASH; the effect of variable Al_2O_3 and MgO/ (MgO + FeO) on mineral stability. *Geological Materials Research*, **3,** 1–42.

Todd, C., 1998. Limits on the precision of geobarometry at low grossular and anorthite content. *The American Mineralogist*, **83,** 1161–1167.

Villeneuve, M. E., Ryan, J. J., Gordey, S. P. & Piercey, S. J., 2003. Detailed thermal and provenance history of the Stewart River area (Yukon-Tanana terrane, western Yukon) through application of SHRIMP, Ar-Ar and TIMS. Geological Association of Canada–Mineralogical Association of Canada Abstracts, 28, 344.

White, D., Colpron, M., Buffett, G. & Roberts, B., 2006. Structural constraints for oil and gas assessment in the Whitehorse Trough: new results from seismic profiling. In: *Yukon Exploration and Geology 2005* (eds Emond, D.S., Bradshaw, G.D., Lewis, L.L. & Weston, L.H.), pp. 315–323. Exploration and Geological Services Division, Indian and Northern Affairs Canada, Whitehorse, Yukon.

Williams, M. L., Jercinovic, M. J. & Terry, M. P., 1999. Age mapping and dating of monazite on the electron microprobe; deconvoluting multistage tectonic histories. *Geology*, **27,** 1023–1026.

Williams, M. L., Jercinovic, M. J. & Johnson, S. E., 2002. Microprobe monazite geochronology; putting absolute time into microstructural analysis. *Journal of Structural Geology*, **24,** 1013–1028.

York, D., 1969. Least squares fitting of a straight line with correlated errors. *Earth and Planetary Science Letters*, **5,** 320–324.

Zhu, X. K., O'Nions, R. K., Belshaw, N. S. & Gibb, A. J., 1997. Lewisian crustal history from *in situ* SIMS mineral chronometry and related metamorphic textures. *Chemical Geology*, **136,** 205–218.

Received 5 December 2006; revision accepted 21 June 2007

APPENDIX: GEOCHRONOLOGICAL METHODS

U-Pb thermal isotope mass spectrometry (TIMS) of titanite

Following the separation of heavy minerals using heavy liquids, samples were passed through a Frantz LB-1J magnetic separator to purify titanite. Titanite crystals were hand-selected for analysis based on criteria that optimized their clarity, consistency of colour, and lack of fractures. Following abrasion, photography, and final mineral selection, mineral fractions were analysed according to methods summarized in Parrish *et al.* (1987). Data were reduced and errors propagated using software written by J. C. Roddick; error propagation was done by numerical methods (Parrish *et al.*, 1987; Roddick, 1987). Error ellipses on concordia diagrams are shown at the 2-sigma (95% confidence) level of uncertainty. Final errors are indicated in Table 3. Linear regressions on discordant arrays of data use a modified York (1969) method that takes into account the scatter of the points about the line (see a discussion in (Parrish *et al.*, 1987). Fraction letters shown on concordia diagrams are keyed to the fraction letters in Table 3.

© 2007 Blackwell Publishing Ltd

U-Th-Pb SHRIMP analysis of monazite

Back-scattered electron (BSE) images of *in situ* monazite grains were acquired on a Cambridge S360 (located at Geological Survey of Canada, Ottawa, and operating at 20 kV accelerating voltage and 2 nA beam current) in order to assess internal structure, facilitate selection of analytical sites, and provide further insight into petrological context.

U-Pb analyses were performed on *in situ* monazite using the SHRIMP II located at the Geological Survey of Canada facility in Ottawa, Canada. Analytical protocols for monazite have been previously described in detail (Stern & Berman, 2000). Selected monazite targets were prepared for *in situ* analysis according to the methods of Rayner & Stern (2002), with the exception that, in order to fit more samples on each of the two epoxy mounts, 3-mm-diameter cores of thin sections were ground to smaller size (with a hand burnisher using surgical hemostats to hold each core) prior to mounting in epoxy. Small plugs of pre-polished laboratory standard monazites (GSC monazite z3345; $^{207}Pb/^{206}Pb$ TIMS age = 1821.0 ± 0.6 Ma (2σ); GSC monazite z2908, $^{207}Pb/^{206}Pb$ TIMS age = 1795.2 ± 0.7 Ma (2σ); Stern & Berman, 2000) were included in both mounts. Analyses were conducted using an O_2^- primary beam. Two different spot sizes were used during the analyses, with diameters of 16 and 12 μm and beam currents of ~0.7 and 0.3 nA respectively. The count rates of 10 isotopes of Ce^+, U^+, Th^+ and Pb^+ were sequentially measured over seven scans with a single electron multiplier and a pulse counting system with dead time of 24 ns. Moderate energy filtering was used to eliminate a known isobar at mass 204 (Stern & Berman, 2000). Off-line data processing was accomplished using customized in-house software. The 1σ external errors of $^{206}Pb/^{238}U$ ratios reported in Table 4 incorporate a ±1.0% error in calibrating the standard monazite. A 0.89% Pb fractionation correction was applied to the $^{207}Pb/^{235}U$ ages. Common Pb correction utilized the measured $^{204}Pb/^{206}Pb$ and the assumed composition of surface Pb (Stern, 1997).

The program ISOPLOT (Ludwig, 2001) was used to generate Concordia plots and weighted mean ages. In order to reliably interpret the age determinations, X-ray maps (Y, Th, U, Ca as a proxy for Pb) were collected with a CHEMICA microprobe at the University of Massachusetts.

© 2007 Blackwell Publishing Ltd